J. Fluid Mech. (1990), *vol.* 219, *pp.* 81–118
Printed in Great Britain

The stress tensor in granular shear flows of uniform, deformable disks at high solids concentrations

By MARIJAN BABIĆ, HAYLEY H. SHEN AND HUNG TAO SHEN

Department of Civil and Environmental Engineering, Clarkson University,
Potsdam, New York 13676, USA

(Received 11 September 1989)

Application of the kinetic theory of gases to granular flows has greatly increased our understanding of 'rapid' granular flows. One of the underlying assumptions is that particles interact only through binary collisions. For a given set of material and flow parameters, as the concentration increases, the transition from a binary collision mode to other modes of interaction occurs. Kinetic theory can no longer be applied. A numerical model is utilized to simulate the mechanical behaviour of a small assembly of uniform, inelastic, frictional, deformable disks in a simple shear flow. There are two objectives: to obtain the 'empirical' constitutive law and to gain insight into the mechanisms that operate in the transitional and quasi-static regimes. In a simple shear flow, spatially and temporally averaged dimensionless stresses $\tau^*_{ij} = \tau_{ij}/(\rho_s D^2 \dot{\gamma}^2)$ are functions of the concentration C, the dimensionless shear rate $B = \dot{\gamma}/(K_n/m)^{\frac{1}{2}}$, and material parameters ζ_n, K_s/K_n and μ. Here $\dot{\gamma}$ is the shear rate, K_n is the normal stiffness of an assumed viscoelastic contact force model, K_s/K_n is the ratio of tangential to normal stiffness, ζ_n is the normal damping coefficient, μ is the friction coefficient, and ρ_s, D and m are the particle density, diameter and mass, respectively. The range of B from 0.001 to 0.0707 was investigated for C ranging from 0.5 to 0.9, with material constants fixed as $\zeta_n = 0.0709$ (corresponding to the restitution coefficient $e = 0.8$ in binary impacts), $K_s/K_n = 0.8$ and $\mu = 0.5$. It is found that for lower concentrations ($C < 0.75$) dimensionless stresses τ^*_{ij} are nearly independent of B, while for higher concentrations ($C > 0.75$) τ^*_{ij} monotonically decreases as B increases. Moreover, their relationship in this regime is well approximated by power law: $\tau^*_{ij} \propto B^{-n_{ij}(C)}$. The powers n_{ij} range from nearly zero for $C = 0.775$ (corresponding to the familiar square power dependency of dimensional stresses on the shear rate in the rapid flow regime), to nearly two for $C = 0.9$ (corresponding to shear-rate independence in quasi-static regime). The intermediate concentration range corresponds to transition. Distinct mechanisms that govern transitional and quasi-static regimes are observed and discussed.

1. Introduction

Mechanical behaviour of dry, cohesionless granular material can be classified into grain-inertia (rapid flow), transitional, and quasi-static (slow flow) regimes (Savage 1982). These regimes are characterized by different transport mechanisms. In the rapid flow regime, principal transport mechanisms are 'kinetic' transport by particle fluctuations and 'collisional' transport by particle interactions (often assumed to be instantaneous, binary collisions). In the quasi-static regime, the principal transport mechanism is developed through a 'network' of contact forces, created by continuous and simultaneous contacts between particles. A complete granular flow theory should include all of the above mechanisms, each of which would become dominant in the appropriate regime. However, most of the research has been concentrated on limiting regimes. A complete theory which would include the transition between limiting regimes is not yet available.

Granular materials are discrete systems that can be viewed as a continuum only upon suitable statistical averaging. Macroscopic behaviour of the system is then described by differential forms of mass, momentum and energy conservation laws. The central problem is the determination of constitutive laws for fluxes of momentum (stresses), mechanical energy (energy diffusion) and energy dissipation over the full range of concentrations and flow conditions. In search of these constitutive equations current research efforts include theoretical, experimental and numerical models.

A number of theories have been developed for rapid granular flows. The most sophisticated are the kinetic theories (Jenkins & Savage 1983; Lun *et al.* 1984; Jenkins & Richman 1985*a*, *b*, 1988) which are developed after Chapman–Enskog's kinetic theory of dense gases. The velocity distribution function is solved by perturbation methods and transport properties are calculated 'exactly'. When applied to a simple shear flow, kinetic theories predict stresses to be proportional to the square of the velocity gradient, as predicted earlier by Bagnold's (1954) simple micromechanical theory. Major assumptions employed are the assumption of 'molecular chaos' (particle positions and velocities are statistically uncorrelated) and the assumption of instantaneous, binary collisions of nearly elastic, smooth, rigid particles (uniform disks or spheres). Thus, these theories are limited to the range of applicability of the above assumptions.

The quasi-static regime (slow deformation of the material) has been studied extensively in connection with the problems of soil mechanics, as reviewed by Spencer (1981). In this regime, the most commonly used approach is based on the continuum theory of soil plasticity. Inertia forces are generally neglected. This approach provides little insight into the micromechanics of the problem.

Several attempts to combine all transport mechanisms have been made (Johnson & Jackson 1987; Savage 1988). These theories are based on the heuristic argument that stresses due to different mechanisms can simply be added together. Total stresses are then equated to the sum of kinetic and collisional stresses (as obtained by kinetic theory) and 'plastic', or 'frictional' contribution (typically assumed to be given by quasi-static Mohr–Coulomb theory). In principle, the plastic part is associated with contact forces, multiple contacts, sliding, rolling and other mechanisms not considered in kinetic theory.

Discrete particle numerical simulations of granular material motion have become a valuable tool for investigation of particulate media behaviour. These models determine the behaviour of an idealized granular material by calculating the motion of individual particles as they interact with each other and the boundaries. Macroscopic properties are then determined by appropriate space and time averaging. This approach originates from ideas and methods of molecular dynamics, which began in 1957 and has undergone extensive development since. A review has been given by Allen & Tildesley (1988). The success of molecular dynamics calculations in predicting equilibrium equations of state and non-equilibrium transport properties has been one of the major motivating factors for the adaptation of these techniques to granular materials.

There are two basic techniques used for the numerical simulation of the behaviour of systems of particles: rigid-particle and soft-particle models. In rigid-particle models collisions are assumed to be instantaneous. Post-collision trajectories are determined from the initial trajectories and an inelastic, frictional collisional operator governing the dynamics of an idealized binary collision. A list of collisions, in order of precedence, is maintained and simulation proceeds by variable time steps between successive collisions. The first rigid-particle model for granular flow was developed by Campbell (1982). Campbell & Brennen (1985*a*, *b*) reported results of Couette and chute flow simulations. Campbell & Gong (1986) performed a detailed study of the stress tensor in a simple shear flow. Hopkins & Shen (1988) have developed Monte Carlo simulation of simple shear flow. Hopkins (1987) has developed a dynamical rigid-particle numerical simulation similar to Campbell's with the motivation of providing the spatial context for the Monte Carlo simulation as well as to provide a check for the two-dimensional air-table experiments of Sanders, Hopkins & Ackermann (1988).

The soft-particle approach requires that collisions be of finite duration. The duration of contact is related to finite particle stiffness which is specified as a particle property. The force at the contact is continuously varying as particles are being deformed. The deformation of the particle is represented as a small overlap. Various contact force models can be incorporated (elastic, viscoelastic, Hertzian, etc.). Forces at all contacts are determined at one instant and Newton's equations of motion are then numerically integrated to obtain new particle positions and velocities. The simulation proceeds by small time steps which are usually kept at a fixed value. This approach can be applied to all configurations, including static and dynamic situations. Cundall and Strack developed the first discrete-particle model based on the soft-particle approach (Strack & Cundall 1978; Cundall & Strack 1979*a*, *b*, 1983; Cundall, Drecher & Strack 1982). Although their calculation method treats the full dynamics of a system of particles, the model was used primarily to investigate the behaviour of granular material undergoing slow, quasi-static deformations. Walton & Braun (1985, 1987) simulated the behaviour of small assemblies of nearly rigid, inelastic, frictional disks undergoing steady-state shearing. Periodic boundaries in all directions were used to simulate simple shear flow. In their study solid fractions were in the range between low and moderately high, resulting mostly in rapid flow conditions.

The present model is patterned after the above-mentioned similar models of Cundall & Strack and Walton & Braun. Earlier versions of the model were successfully used to reproduce most of the existing results concerning special quasi-static or dynamic problems (complex two-dimensional configurations, rectangular wall-bounded systems under external loading, uniform rectilinear flows: Couette, gravity, etc.). These results as well as details of the code are described in Babić (1988).

In this work, results for the simple shear flow of uniform disks at high solid fractions are reported. From these numerical results an 'empirical' relationship between stresses, shear rate and concentration can be derived. In the subsequent text, this relationship will be referred to as the phenomenological constitutive equation. It is not a general constitutive equation but only one important particular case. If a plausible form for the general constitutive equation were proposed, present

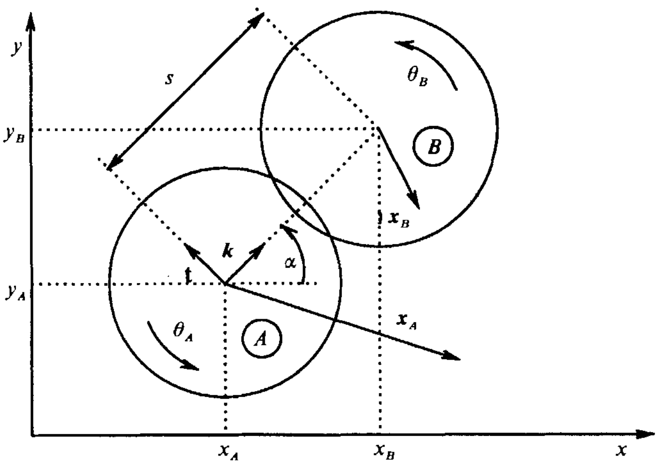

FIGURE 1. Contact between two particles.

results could be used to determine unknown coefficients in the general constitutive equation. In addition, these numerical results also provide an insight into the physical behaviour of granular materials in transitional and quasi-static regimes which is not well understood.

2. Numerical model

The simulation proceeds by repeating a set of calculations (calculation cycle) for each time step. The calculation cycle includes routines to search for all existing contacts, to calculate forces at all contacts from the force-displacement law, to integrate equations of motion for all particles and to obtain new positions and velocities, to handle periodic boundary conditions and to update statistical summations.

2.1. *Contact between particles*

The contact of two disks, A and B, is shown in figure 1. The position vectors of the centres of disks A and B are represented as $\boldsymbol{x}_A$ and $\boldsymbol{x}_B$. The velocity vectors of centres of disks A and B are represented as $\dot{\boldsymbol{x}}_A$, $\dot{\boldsymbol{x}}_B$, and the angular velocities are denoted as $\dot{\theta}_A$ and $\dot{\theta}_B$, taken positive in the counterclockwise direction. The unit vector $\boldsymbol{k}$ is defined to be pointing from the centre of disk A to the centre of disk B and the unit vector $\boldsymbol{t}$ is obtained by a counterclockwise rotation of $\boldsymbol{k}$ through 90°, i.e.

$$\boldsymbol{k} = \frac{\boldsymbol{x}_B - \boldsymbol{x}_A}{|\boldsymbol{x}_B - \boldsymbol{x}_A|} = (\cos\alpha, \sin\alpha); \quad \boldsymbol{t} = (-\sin\alpha, \cos\alpha), \tag{1}$$

where α is the angle between the contact normal $\boldsymbol{k}$ and the x-axis.

Points P_A and P_B are defined as the points of intersection of the line connecting the disk centres with the boundaries of disks A and B, respectively. The relative displacement at the contact point C is determined by the integration of the relative velocity. The relative velocity at the contact is defined as the relative velocity of point P_A with respect to P_B, which can be expressed as

$$\boldsymbol{V}_{AB} = (\dot{\boldsymbol{x}}_A - \dot{\boldsymbol{x}}_B) + R(\dot{\theta}_A + \dot{\theta}_B)\,\boldsymbol{t}, \tag{2}$$

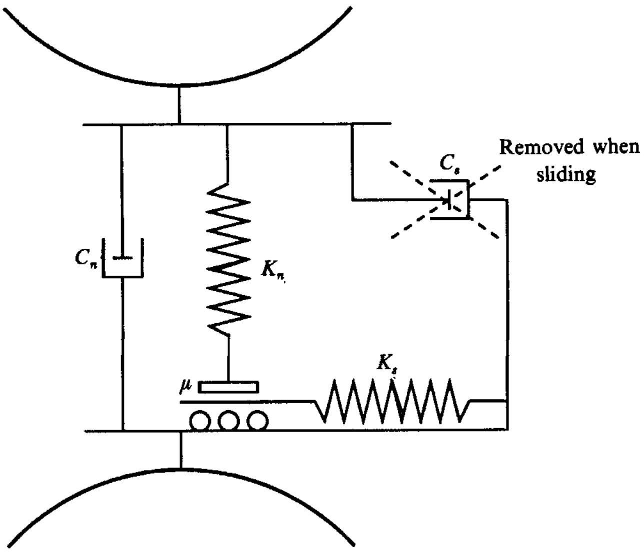

FIGURE 2. Contact force model.

where R is the particle radius. The relative displacement rates in normal and tangential directions $\dot{n}$ and $\dot{q}$ are the projections of $\boldsymbol{V}_{AB}$ onto $\boldsymbol{k}$ and $\boldsymbol{t}$, respectively,

$$\dot{n} = \boldsymbol{V}_{AB} \cdot \boldsymbol{k}; \quad \dot{q} = \boldsymbol{V}_{AB} \cdot \boldsymbol{t}. \tag{3}$$

The contact force model (force–displacement law) implemented in the present model is the same as the one used in Cundall & Strack (1979*a*, *b*). The schematic representation of this contact force model is shown in figure 2.

The force in the normal direction is modelled as viscoelastic (damped harmonic oscillator). It consists of an elastic (spring) contribution and viscous damping (dashpot) contribution. The force in the tangential direction is modelled as viscoelastic below the friction limit (non-sliding contact), and frictional at the friction limit (sliding contact). The friction limit is assumed to be given by the Mohr–Coulomb law. The normal particle stiffness k_n is in principle related to a particle's modulus of elasticity E. Effective contact stiffnesses in the normal and tangentional directions K_n and K_s are obtained from particle stiffnesses k_n and k_s. Using the analogy with springs connected in series, effective contact stiffnesses for identical particles are $K_n = \frac{1}{2}k_n$ and $K_s = \frac{1}{2}k_s$. The normal and shear spring forces at time step N are obtained as

$$F_n^N = F_n^{N-1} + K_n \dot{n}^{N-\frac{1}{2}} \Delta t, \tag{4}$$

$$F_s^N = F_s^{N-1} + K_s \dot{q}^{N-\frac{1}{2}} \Delta t. \tag{5}$$

The contact damping operates on the relative velocities at the contacts. Damping forces D_n and D_s are proportional to components of relative velocities $\dot{n}$ and $\dot{q}$. Damping forces are evaluated as

$$D_n = 2\zeta_n (mK_n)^{\frac{1}{2}} \dot{n}; \quad D_s = 2\zeta_s (mK_n)^{\frac{1}{2}} \dot{q}, \tag{6}$$

where ζ_n and ζ_s are (dimensionless) coefficients of viscous contact damping in the normal and tangential directions, respectively, and m is the particle mass. Dimensional coefficients of damping are denoted as $C_n = 2\zeta_n (mK_n)^{\frac{1}{2}}$ and

$C_s = 2\zeta_s(mK_n)^{\frac{1}{2}}$. On the basis of a theoretical solution for binary contact (collision), an explicit relationship between the normal damping coefficient ζ_n and coefficient of restitution e can be found to be (Babić 1988):

$$\zeta_n = \frac{-\ln e}{(\pi^2 + \ln^2 e)^{\frac{1}{2}}}. \tag{7}$$

For non-binary interactions the concept of a restitution coefficient is not meaningful. The duration of binary contact was also obtained by Babić (1988) as

$$t_c = \frac{\pi}{[(2K_n/m)(1-\zeta_n^2)]^{\frac{1}{2}}}. \tag{8}$$

Thus, the duration of collision is independent of impact velocity.

A Coulomb-type friction law is incorporated as follows. If the magnitude of the shear force, found from (5), is larger than $(F_s)_{\max} = \mu F_n$, then the shear force is set equal to $(F_s)_{\max}$, with the direction always opposite to the relative tangential velocity at the contact $\dot{q}$. Here μ denotes the interparticle friction coefficient. In that case, the viscous damping in the shear direction is not applied, i.e. $D_s = 0$.

Once all resultant forces and moments acting on each particle are obtained, new velocities and positions of all particles are obtained by numerical integration of Newton's second law. The time-centred finite-difference scheme (leap-frog algorithm) is used to allow explicit numerical integration of the equations of motion.

2.2. *Simple shear flow set-up*

Shear flow of a small assembly of particles is simulated using the periodic boundary conditions, which is a standard technique of non-equilibrium molecular dynamics (Allen & Tildesley 1988). An assembly of N particles is placed in a shear cell centred at the origin of a fixed coordinate system (x_1, x_2). This cell is referred to as the primary calculation cell. The width and height of the primary cell are denoted as a and b, respectively. The primary cell is surrounded by an infinite array of 'image cells'. Each image cell is an exact copy of the primary cell (each particle in the primary cell has its 'clone' in each image cell). The primary cell and the adjacent image cells are connected by periodic boundaries. Periodic boundary conditions operate in such a way that if a particle moves out of the primary cell, its clone automatically enters from the opposite image cell. Thus, the number of particles in the cell is always conserved.

Shear flow of the particle assembly in the primary cell is achieved by the motion of the adjacent layers of image cells in the opposite directions (figure 3). The relative velocity of two adjacent layers of cells is denoted as V. The apparent shear rate is defined as $\dot{\gamma} = V/b$. Depending on the flow conditions (mostly on density), the apparent shear rate $\dot{\gamma}$ may or may not be the same as the local velocity gradient. At low densities, shearing of the particle assembly typically results in uniform shear conditions, the mean velocity profile is continuous, and $\dot{\gamma}$ is equal to the local velocity gradient $\mathrm{d}U_1/\mathrm{d}x_2$ (figure 3*b*). At high densities, a discontinuity in the mean velocity profile typically occurs and the local velocity gradient is not well defined. In the following presentation of results, $\dot{\gamma}$ is always to be interpreted as defined, i.e. as an apparent shear rate.

The simulation set-up described above roughly corresponds to physical experiments in shear cells with rough boundaries. Two notable differences are: (i) the dilation of an assembly is prevented (the cell area and the number of particles are

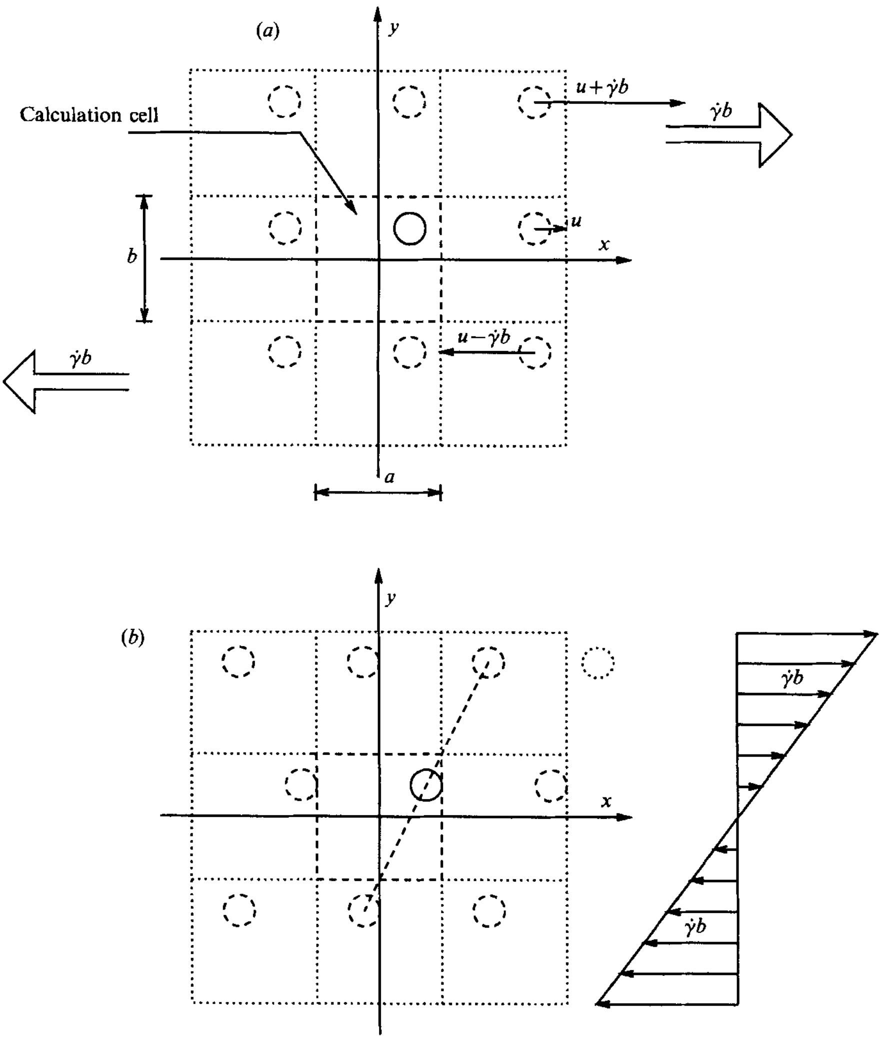

FIGURE 3. Simple shear flow set-up: (*a*) initial configuration ($t = 0$); (*b*) simple shear flow (uniform shearing, $t > 0$).

strictly constant); and (ii) there can be no net flux of energy across periodic boundaries, while in physical experiments energy can flow towards the solid wall or away from it.

2.3. *Statistical averaging*

Space averaging is used to determine instantaneous values of various quantities averaged over all particles in the primary computational cell. In Appendix A, the instantaneous mechanical energy equation is derived. The result is

$$\frac{\mathrm{d}}{\mathrm{d}t}(T+V) = \tau_{ji}D_{ij} - \Gamma, \tag{9}$$

where the Cartesian components of D_{ij} are $D_{12} = \dot{\gamma}$, $D_{11} = D_{22} = D_{21} = 0$. In the case of uniform shearing (low densities), D_{ij} may be identified with the local velocity

gradient tensor. $T = T_t + T_r$ is the kinetic energy per unit volume with respect to mean flow, V is the potential energy per unit volume, $\tau_{ij} = \tau^{k}_{ij} + \tau^{c}_{ij}$ is the complete stress tensor and Γ is the rate of energy dissipation per unit volume. These terms are defined as follows:
translational fluctuation kinetic energy per unit volume

$$T_t = \frac{1}{A} \sum_{p=1}^{N} \tfrac{1}{2} m (u_i'^p u_i'^p); \tag{10}$$

rotational kinetic energy per unit volume

$$T_r = \frac{1}{A} \sum_{p=1}^{N} \tfrac{1}{2} I \dot{\theta}_p^2; \tag{11}$$

potential energy per unit volume

$$V = \frac{1}{A} \left\{ \sum_{c=1}^{M} \left[\frac{F_n^2}{2K_n} \right] + \sum_{c=1}^{M_1} \left[\frac{F_s^2}{2K_s} \right] \right\}; \tag{12}$$

rate of dissipation per unit volume

$$\Gamma = \frac{1}{A} \left\{ \sum_{c=1}^{M} [C_n \dot{n}^2] + \sum_{c=1}^{M_1} [C_s \dot{q}^2] + \sum_{c=1}^{M_2} [F_s |\dot{q}|] \right\}; \tag{13}$$

kinetic stress tensor

$$\tau^{k}_{ij} = -\frac{1}{A} \sum_{p=1}^{N} m u_i'^p u_j'^p; \tag{14}$$

contact stress tensor

$$\tau^{c}_{ij} = \frac{1}{A} \sum_{c=1}^{M} D(k_i F_j), \tag{15}$$

where A is the flow field (cell) area, N is the number of particles in A, $M = M_1 + M_2$ is the total number of contacts inside A, M_1 is the number of non-sliding contacts and M_2 is the number of sliding contacts. The fluctuation velocity of particle p with respect to the mean shear flow, which appears in translational energy and kinetic stress terms, is defined by $u_i'^p = u_i^p - D_{ij} x_j^p$. The above expressions are used for numerical evaluation of instantaneous spatially averaged system properties during the simulation. One important result of the derivation given in Appendix A is to show that the expression for the contact stress tensor (15) is valid even if the assumption of negligible inertia (as in, for instance, Cundall *et al.* 1982) is not employed.

Time averaging was performed in the following way. The cumulative time averages of interesting quantities were monitored during the run, and the system was assumed to be in steady state when cumulative averages approached constant values within a certain accuracy. The cumulative time average of the quantity φ over nt time steps is defined as

$$\bar{\varphi}(nt) = \frac{1}{nt} \sum_{it=0}^{nt} \varphi(it). \tag{16}$$

Further check to determine whether the system has arrived at a steady state from a dynamical point of view comes from performing a time averaging of the energy equation (9), which yields

$$\bar{\tau}_{21}\dot{\gamma} = \bar{\Gamma}, \tag{17}$$

i.e. in steady state the average shear stress power is balanced by the average rate of energy dissipation. Typically, this condition was satisfied within 5% in actual simulations.

3. Analysis of results

3.1. *Dimensional analysis*

Basically, the problem amounts to finding the relationship between stresses τ_{ij} and the following variables: shear rate $\dot{\gamma}$, number density $n = N/A$ (or the nominal concentration $C = \frac{1}{4}nD^2\pi$), particle diameter D, particle mass m (or solid density ρ_s), normal and tangential contact stiffnesses K_n and K_s, normal and tangential damping coefficients ζ_n and ζ_s and coefficient of friction μ. Namely,

$$\tau_{ij} = f_{ij}(\dot{\gamma}, C, D, m, K_n, K_s, \zeta_n, \zeta_s, \mu; N). \tag{18}$$

Applying dimensional analysis to the above yields

$$\tau^*_{ij} = f^*_{ij}(B, C, \zeta_n, \zeta_s, K_s/K_n, \mu; N), \tag{19}$$

where $\tau^*_{ij} = \tau_{ij}/(\rho_s D^2\dot{\gamma}^2)$ and $B = \dot{\gamma}/(K_n/m)^{\frac{1}{2}}$. The effect of sample size is indicated by the possible dependence of stresses on the number of particles N.

The role of parameter B should be discussed at this point. The dimensional analysis clearly indicates that dimensionless stresses τ^*_{ij} are functions of B only, when the number density n (or C) and material parameters ζ_n, ζ_s, K_s/K_n and μ are held constant. For a constant m, say $m = 1$, B can be varied in two ways: holding K_n constant and varying $\dot{\gamma}$, or holding $\dot{\gamma}$ constant and varying K_n. The first way corresponds to the same material being sheared at a slower or faster rate. The second way corresponds to softer or harder particles being sheared at a constant rate. The theoretical limit of particle hardness is $K_n \rightarrow \infty$ ($B \rightarrow 0$), corresponding to perfectly hard (rigid) particles. In this case, particles interact via binary collisions only, and stresses are invariably proportional to the square of the shear rate. This regime of behaviour is termed 'rapid flow'. As K_n decreases, particles become softer and softer, and the percentage of multiple contacts increases. The reason for this is that the collision duration t_c, given by (8), increases as K_n decreases. Therefore, the probability that another particle will 'join' a colliding couple is proportionally higher. In this case, the flow is no longer rapid.

At sufficiently high solid volume fractions, soft particles interact through continuous, simultaneous contacts, creating a network of contact forces. Stresses are eventually going to become shear-rate independent, and this regime of behaviour is termed 'quasi-static' or, often, 'slow flow'. In other words, for fixed C, the behaviour changes from the rapid towards the quasi-static regime as B increases. However, as mentioned earlier, B can also be increased by increasing the shear rate $\dot{\gamma}$, at constant K. In this case, the behaviour changes from the rapid towards the quasi-static regime as the shear rate increases. This contradicts the usual notion that rapid flow is fast flow and quasi-static flow is slow flow. It is really the other way around, the flow is becoming more and more 'rapid' (binary collisions dominant) for slower and slower shear rates; and more and more quasi-static (multiple contacts dominant) for faster and faster shear rates at constant concentration. This conjecture will be verified by simulation results.

The simple shear flow simulation used in this study corresponds to a 'constant-volume' type of experiment. The number of particles in the cell and the cell area are fixed. The concentration (apart from the minute fluctuations associated with particle deformations) is constant. The conclusion stated above that the flow characteristics tend to change from rapid to quasi-static with increasing shear rate is valid as long as concentration is constant. In the experimentally more common situation, where the normal force is held constant, the particle assembly responds with dilation to the increase in the shear rate. The dilation is responsible for the increase of volume and thus the decrease in concentration. At lower concentrations, naturally, flow tends to be more rapid. Therefore, in a 'constant-pressure' type of experiment, the system will move from the slow towards rapid flow type of behaviour, owing to decrease in concentration caused by dilation. This trend can be indirectly detected from simulation results. It should be noted, however, that constant-pressure numerical experiments would be impossible to perform in a consistent manner over a full range of concentrations.

3.2. *Experimental procedure*

A complete set of numerical experiments with $N = 30$ particles, has been performed for all combinations of $C = 0.5, 0.6, 0.7, 0.75, 0.775, 0.8, 0.825, 0.85, 0.875, 0.9$ and $B = 0.001, 0.01, 0.0707$.

In all runs B was varied by changing K_n and holding mass $m = 1$, and the shear rate $\dot{\gamma} = 1$. A few test runs were performed with the same B using different combinations of K_n, m and $\dot{\gamma}$ in order to verify conclusions concerning dimensional analysis and the results were identical.

The time step used was obtained as a fraction ($\frac{1}{50}$) of the duration of the normal binary contact time t_c given by (8). The normal damping coefficient is selected as $\zeta_n = 0.0709$, such that the corresponding restitution coefficient for binary impacts becomes $e = 0.8$, according to (7). The friction coefficient is $\mu = 0.5$. The ratio of shear to normal stiffness $K_s/K_n = 0.8$, and the shear damping coefficient ζ_s is set to zero. The dimensionless time step $\mathrm{d}t^* = \dot{\gamma}\,\mathrm{d}t = \dot{\gamma}t_c/50 = 0.0445B$.

The particles' radii are set to unity and the cell dimensions are selected such that a specified nominal concentration is obtained for the given number of particles. Initially, particles are placed in regular hexagonal packing. Initial velocities of particles consist of randomly oriented fluctuation velocity of magnitude v' and a mean component in the x-direction which is proportional to the shear rate and the particles' initial y-coordinate. The approach to uniform shear conditions is enhanced by this initial mean velocity profile. The total initial momentum in the system is set to zero by subtracting from each particle velocity the sum of all initial fluctuation velocity vectors divided by the number of particles. The magnitude of the initial fluctuation velocity v' is an input variable, which is selected to achieve an estimated average fluctuation particle velocity during the run. With a good choice of v', the approach to steady state takes a shorter time.

Simulations were run until cumulative-time-averaged mean stresses approached an approximately constant value. Typically, for $B = 0.001$ this would require between 500000 and 2000000 time steps, for $B = 0.01$ between 200000 and 500000 time steps and for $B = 0.0707$ between 50000 and 100000 time steps. Obviously, the most expensive runs were for $B = 0.001$, where 2000000 steps or more than 10 hours

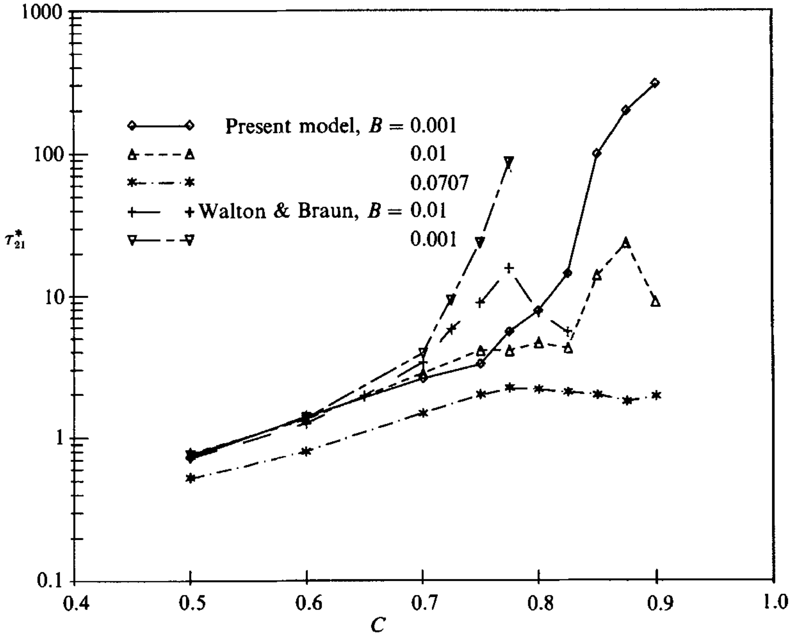

FIGURE 4. Dimensionless shear stress *vs.* C.

of CPU time on a Gould 9080 was required. Simulations with values of B lower than 0.001 were not feasible on this computer.

Results of the simulation consist of cumulative mean values for all components of kinetic and contact stresses, kinetic energy per unit volume (translational and rotational), potential energy per unit volume (due to normal springs and shear springs), dissipation rate per unit volume (due to normal damping, shear damping and friction), mean angular velocity, fluctuation velocity distribution, frequency of broken contacts (collisions), coordination number (mean number of contacts per particle), contact number percentages, contact angle distribution, fabric tensor components, fraction of slipping contacts, etc. The most important of these results are tabulated in tables 1–3 in Appendix B. In addition to these mean values, a time history of instantaneous cell-averaged values is available for most of these quantities.

3.3. *Phenomenological constitutive equations*

The objective of this study is, once again, to obtain a relationship between stresses, apparent shear rate, concentration and material properties. This relationship is referred to as the phenomenological constitutive equation. Since material properties are held constant, in this study only the dependence of dimensionless stresses on B and C was investigated. Furthermore, all results are obtained with the number of particles $N = 30$. The effect of sample size (i.e. N) on the results will be a part of future work.

Time-averaged dimensionless stresses τ_{ij}^* are plotted versus concentration C in figures 4, 6, and 8, and versus parameter B (dimensionless shear rate) in figures 5, 7 and 9. For comparison, data of Walton & Braun (1985) are also shown. They have applied a similar computer model to the same problem of simple shear flow of uniform disks, using the same number of particles, $N = 30$. They have investigated a low to moderately high concentration range (0.025–0.825), resulting mostly in

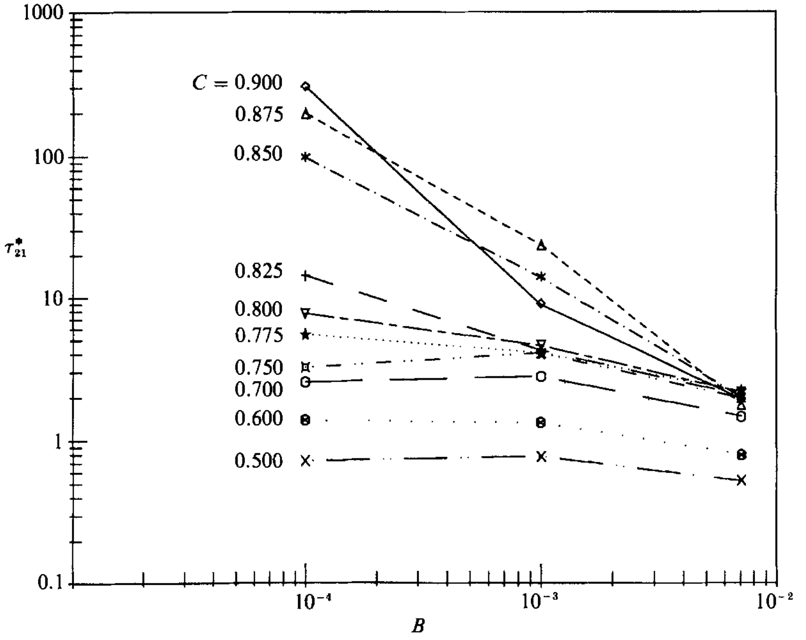

FIGURE 5. Dimensionless shear stress *vs.* B.

rapid flow conditions. At $C = 0.8$ they have observed the onset of transition, but have not pursued their investigation any further. Results of the present model compare very well with the data of Walton & Braun (1985) for lower concentrations, but begin to deviate for higher concentrations. It should be noted that they performed two runs with different initial conditions for each case they investigated. The difference in results increases with concentration. In our figures, for clarity, only mean values of their results are shown. Actually, the comparison with the lower limits of their calculated results is quite good even for high concentrations.

The major difference between the model of Walton & Braun (1985) and present model is the force-displacement law (contact force model). In their model, the normal force is described by a partially latching spring model. The force-displacement law has different slopes for loading and unloading portions of an impact. Thus, the normal force exhibits a position-dependent hysteresis which results in a coefficient of restitution of less than unity for normal impacts. The tangential friction force model is based on theoretical models for friction forces acting between elastic spheres in contact developed by Mindlin & Deresiewitz (1953). In the regime where binary contacts are dominant, the effect of different contact-force models is small. In fact, it can be shown analytically that for normal binary contacts, the results of the two models should be exactly the same. However, differences in treatment of inelasticity and tangential force component have led to larger discrepancies in the regime where multiple, continuous contacts are dominant.

In figures 5, 7, and 9, dimensionless stresses τ^*_{ij} are plotted versus B on log–log scales for different values of C. It can be seen from these figures that for lower concentrations ($C < 0.75$) dimensionless stresses are nearly independent of B in the range from $B = 0.001$ to $B = 0.01$, but decrease for $B = 0.0707$. Theoretically, on these curves, there should be an asymptote (hard-disk point) as $B \rightarrow 0$. For $C = 0.5$ and 0.6 it appears that this asymptote has already been reached, since stresses for

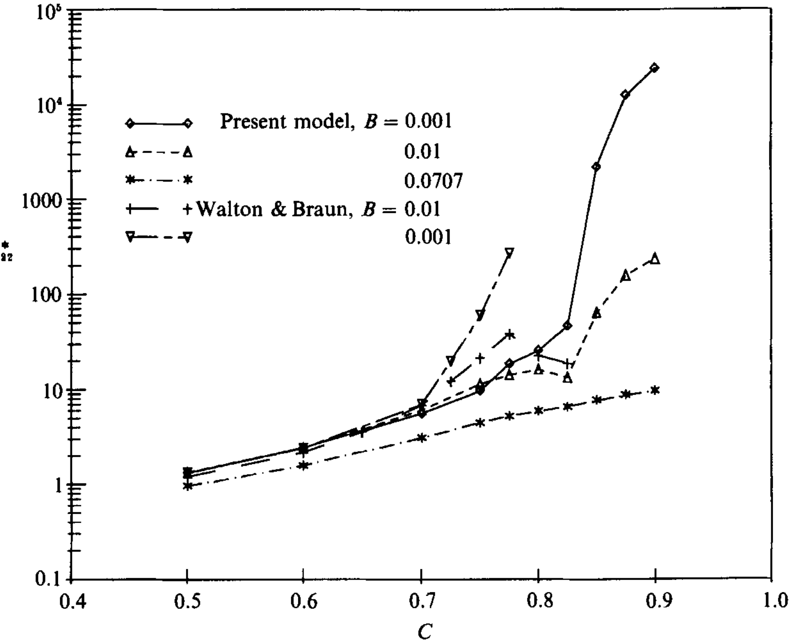

FIGURE 6. Dimensionless transverse normal stress *vs*. C.

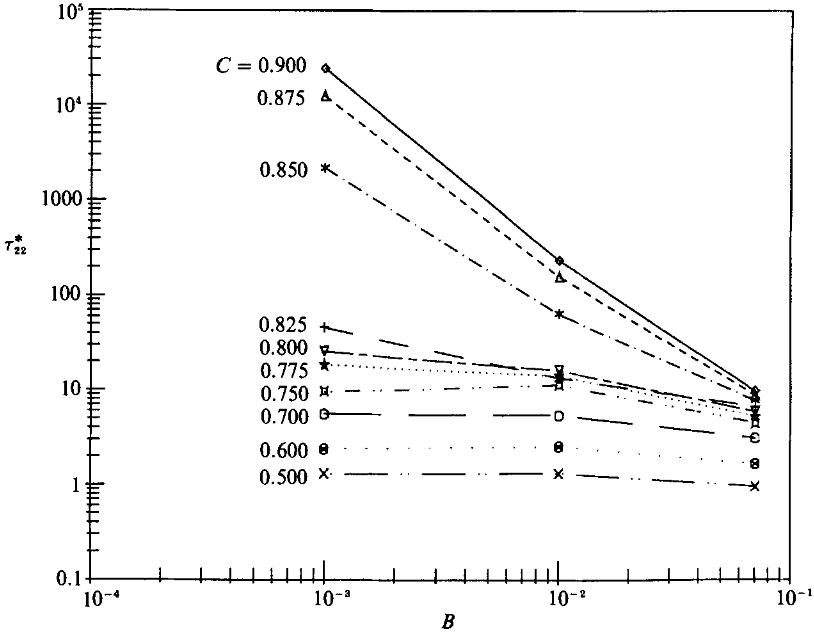

FIGURE 7. Dimensionless transverse normal stress *vs*. B.

$B = 0.001$ and $B = 0.01$ are nearly the same. For $C = 0.7$ and 0.75, surprisingly, stresses for $B = 0.01$ are slightly higher than stresses for $B = 0.001$. This may be due to statistical uncertainties. It is also not certain whether the hard-disk asymptote has been reached in these cases. For higher concentrations ($C > 0.775$), τ^*_{ij} monotonically decreases as B increases. For $C = 0.775$, 0.8 and 0.825 it seems that

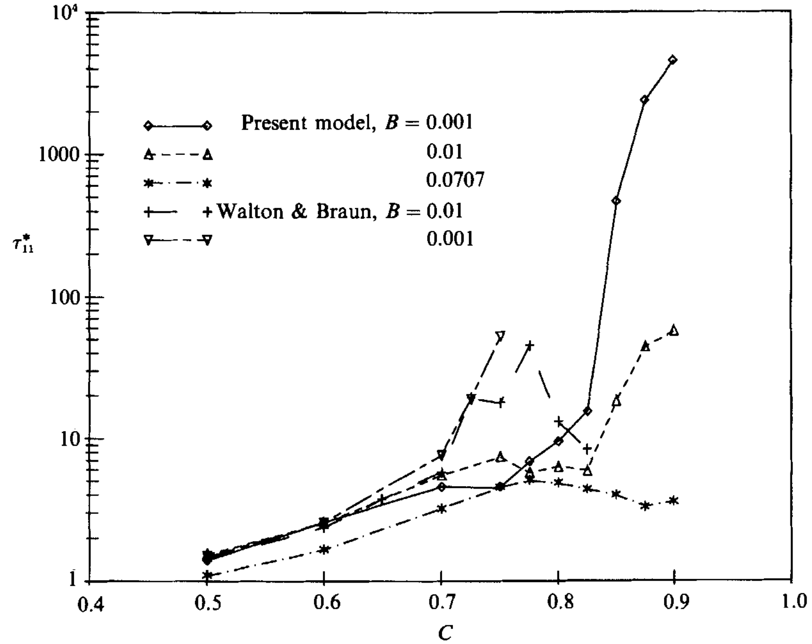

FIGURE 8. Dimensionless streamwise normal stress *vs*. C.

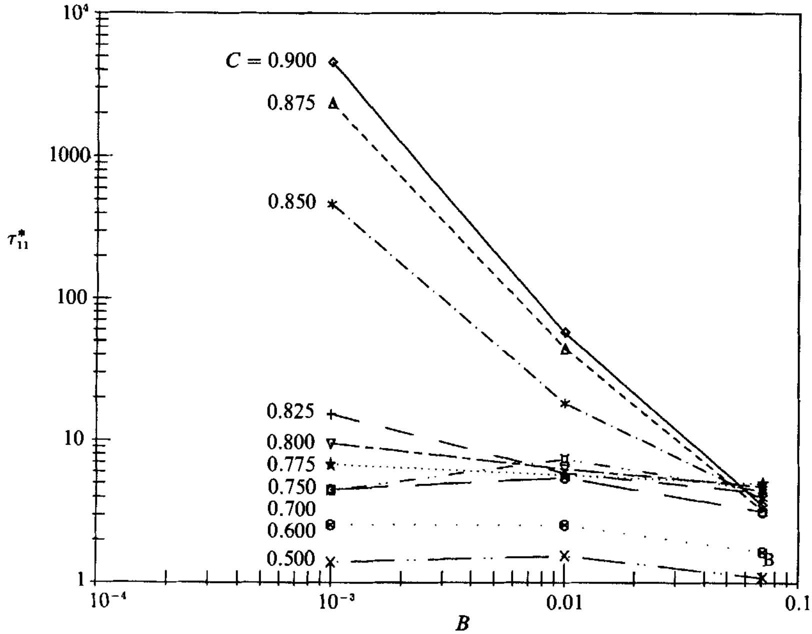

FIGURE 9. Dimensionless streamwise normal stress *vs*. B.

the hard-disk asymptote would probably be reached with one more order of magnitude decrease in B ($B \approx 0.0001$). For $C = 0.85$, all stress components increase sharply, and the system undergoes a phase-change type of transition. For high C ($C = 0.85, 0.875$ and 0.9), the hard-disk flow may not be possible at all, and the stresses may be increasing as B decreases all the way to zero. The steepness of the (τ^*, B)-

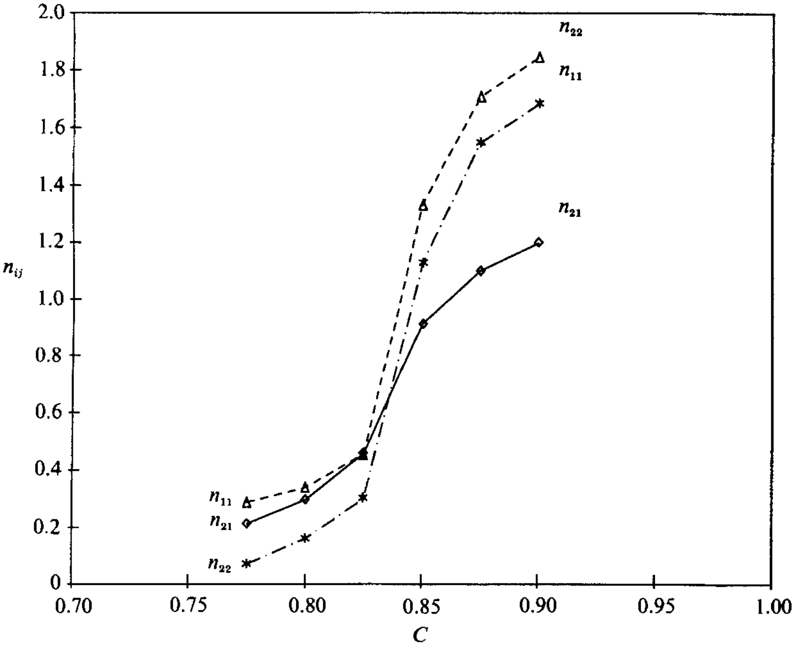

FIGURE 10. Power n_{ij} *vs*. C.

curves, which increase with C, clearly indicates this trend. Setting the curvature aside for the time being, one can quite well approximate (τ^*, B)-curves by straight lines in the range of B that was investigated (0.001–0.0707) for $C > 0.775$. This suggests the functional form

$$\tau^*_{ij} = a_{ij}(C)B^{-n_{ij}(C)}, \tag{20}$$

where a_{ij} and n_{ij} can be obtained for each C by regression analysis. Recasting (20) in dimensional form, it then follows that

$$\tau_{ij} = a_{ij}(C)\rho_s D^2 \dot{\gamma}^{2-n_{ij}(C)}(K/m)^{n_{ij}(C)/2}. \tag{21}$$

The importance of this approach now becomes apparent. The stresses are proportional to the shear rate to the power $(2-n_{ij})$. As C increases, so does n_{ij}, and the resulting stress-shear-rate dependence changes from a power of two (rapid flow) for low concentration to a lower and lower power, eventually reaching $n_{ij} = 2$ for very high C, corresponding to a quasi-static, rate-independent limit. Note that n_{ij} and especially a_{ij} could depend on the sample size (or the number of particles N).

In order to quantify these considerations, a regression analysis was performed on the set of three $(\log \tau^*, \log B)$ data points to obtain a_{ij} and n_{ij} for each C. This analysis is given in table 4 in Appendix B. Results are plotted in figures 10 and 11. Figure 10 shows the variation of n_{ij} with C, and figure 11 shows the variation of a_{ij} with C. It can be seen that all $n_{ij}(C)$ curves are S-shaped, asymptotically approaching the rapid-flow limit $n_{ij} = 0$ for low concentrations and quasi-static limit $n_{ij} = 2$ for high concentrations. In fact, for $C = 0.775$, $n_{21} = 0.214$, $n_{11} = 0.072$, $n_{22} = 0.290$, what is a relatively small departure from a second-power shear-rate dependence (rapid flow). On the other hand, for $C = 0.9$, $n_{21} = 1.198$, $n_{11} = 1.684$, $n_{22} = 1.845$, representing what is relatively close to the theoretical quasi-static rate independent limit.

Phenomenological forms of constitutive equations for transition are thus given by

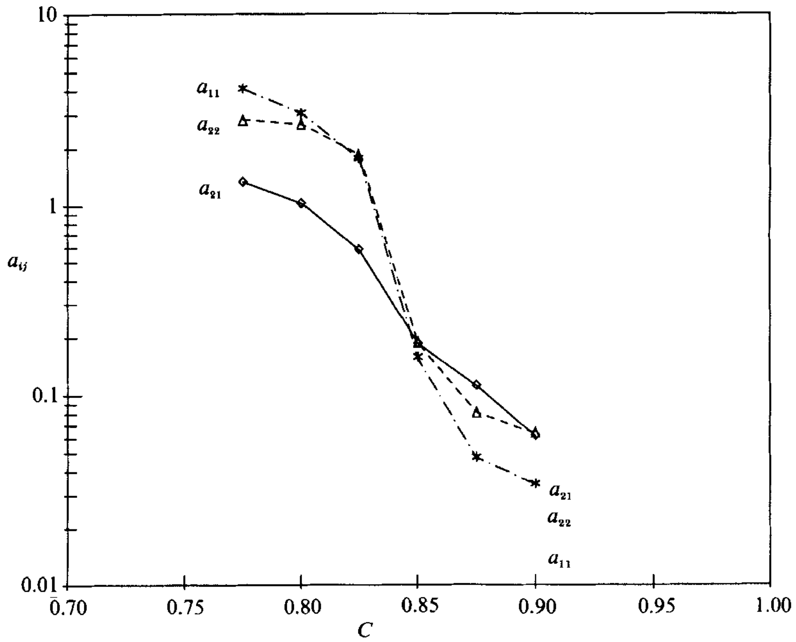

FIGURE 11. Coefficient a_{ij} *vs*. C.

(21) with functions $n_{ij}(C)$ and $a_{ij}(C)$ tabulated in table 4. If so desired, these functions could be fitted with some polynomial expression. These equations are applicable to the range of C approximately from 0.775 to 0.900. For lower C, an appropriate rapid-flow equation may be used, and for higher C an appropriate quasi-static equation may be used, provided that they match the above relationship at end points.

The range of applicability of these equations with respect to B is not quite certain. Strictly speaking, they are applicable only to the range $B = 0.001$–0.0707 that was investigated. Therefore, if the range, say, $B = 10^{-5}$–10^{-3} were investigated next, the coefficients a_{ij} and n_{ij} would probably be different. However, simulations with such values of B are at present not feasible and it is hoped that extrapolation of present results to lower B range would still give a reasonable estimate.

The effect of sample size (or N) may be important, especially at high concentrations. As will be shown in the following section, at high concentrations all of the shearing takes place in a thin region (rolling layer) about which 'solid' blocks of granular material move in opposite directions with relative velocity V. In this case, the apparent shear rate $\dot{\gamma} = V/b$ cannot be associated with the local velocity gradient (which is equal to zero within the blocks and proportional to V/D at the rolling layer). The apparent shear rate is directly affected by changing N and thus the height of the shear cell b. If a significant dependence of results on the sample size were found, perhaps a different non-dimensionalization in the non-uniform shearing case (with B redefined using $\dot{\gamma} = V/D$) would be more appropriate. However, the investigation of the N-effect is postponed for a future study.

The power-law dependence, (20), of τ_{ij} on B (and thus on V), with powers n_{ij} decreasing from 2 to 0 as concentration increases, is an important result which describes the response of stresses to the rate of shearing in the transitional regime. This type of relationship is expected to be valid for different sample sizes as well.

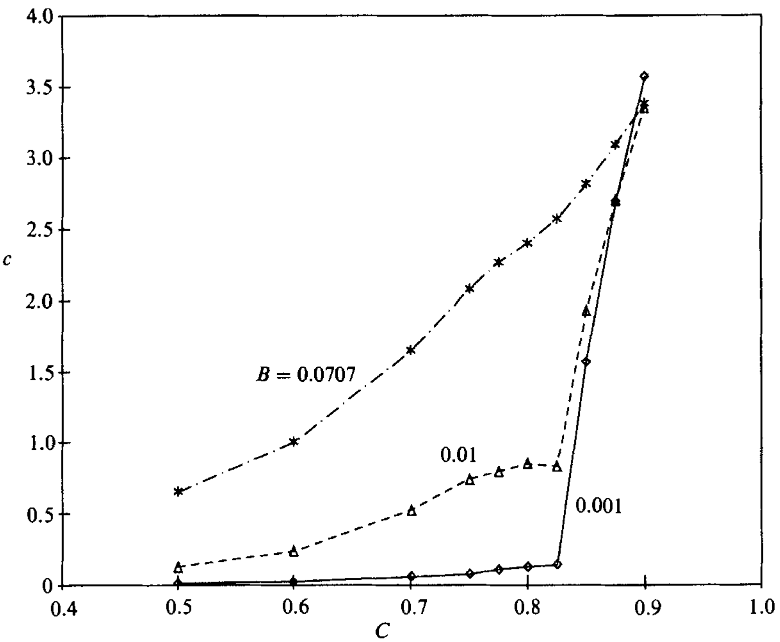

FIGURE 12. Coordination number *vs.* C.

3.4. *Discussion of transition*

One of the major characteristics of rapid flow is that the dominant mode of particle interaction is binary collisions. In order to establish whether a certain flow is indeed in the rapid regime, consider the relationship of the coordination number c and collisional frequency f, both of which are measured during the simulation. The collisional frequency f is defined as the average number of collisions per particle per unit time. The coordination number c is defined as the average number of contacts per particle. If all contacts were binary, then c could also be interpreted as the probability that a particle is undergoing a binary contact (collision) at a given instant. This probability is equal to the ratio of time spent in contacts per unit time, which is equal to ft_c, where t_c is the duration of a binary contact. The duration of binary contact is given by (8), determined analytically. Hence, in the binary collision regime $c/ft_c = 1$. The degree by which this relationship is violated in an actual simulation indicates a departure from the binary collision regime.

The elements of this diagnostic (c, f and the ratio c/ft_c) are tabulated among other quantities in tables 1–3. It can be seen that for $B = 0.001$, $c/ft_c \approx 1$ for low concentrations (0.5, 0.6, 0.7), then slowly increases but is still within 10% deviation for $C = 0.75$. For $B = 0.01$, $c/ft_c \approx 1$ for $C = 0.5$ and 0.6; then has deviated by more than 10% from 1 by $C = 0.7$ and by about 50% for $C = 0.75$–0.825. For $B = 0.0707$, deviation is already large at $C = 0.5$. The marginal concentration for which flow can be called rapid is denoted as C_r. It can be (arbitrarily) defined as the concentration for which the deviation of c/ft_c from 1 is, say, exactly 10%. Apparently, C_r increases as B decreases: for $B = 0.001$, $C_r \approx 0.75$; for $B = 0.01$, $C_r \approx 0.65$, and for $B = 0.0707$, $C_r < 0.5$.

The coordination number c is plotted versus C in figure 12. From this figure it can be clearly seen that system undergoes a phase-change transition (sharp jump in the coordination number) between $C = 0.825$ and 0.85 for both $B = 0.001$ and $B = 0.01$.

Actually, if this interval was further discretized and more runs performed for intermediate concentrations, the exact location of the phase-change transition would be determined. One can speculate that the phase change for $B = 0.001$ occurs for slightly lower C than for $B = 0.01$. This is due to the effect of particle deformations (overlaps), which effectively reduce mean solid volume fraction and allow more void space for shearing. This reduction is more significant for higher B (softer particles). The location of phase change is denoted as C_{pc}. From the location of phase change towards higher concentrations the material is in fact solidified. Large crystallized regions can be observed. Such a structure is characteristic for the uniform size distribution considered here. However, for a non-uniform size distribution, the structure of the particle assembly could be qualitatively different and the location of phase change would depend on details of size distribution. In general, the phase transition would in this case occur at higher concentrations.

From the location of phase change towards higher concentrations the coordination number increases sharply, approximately linearly, for both $B = 0.001$ and 0.01. For $C = 0.9$, the average coordination number is about 3.5. Obviously, if the concentration is further increased, beyond close hexagonal packing ($C = 0.907$), the coordination number would reach its maximum value of 6, and flow would become fully quasi-static. The concentration for which flow becomes fully quasi-static (powers $n_{ij} \rightarrow 2$) is denoted as C_{qs}.

Based on previous discussion, the transitional flow can be classified into two types: type A, prior to phase change and type B, after phase change. The complete flow classification is presented below:

(i) $C < C_{\mathrm{r}}$ – rapid flow (percentage of multiple contacts insignificant);

(ii) $C_{\mathrm{r}} < C < C_{\mathrm{pc}}$ – transitional flow, type A (prior to phase change: percentage of multiple contacts significant);

(iii) $C_{\mathrm{pc}} < C < C_{\mathrm{qs}}$ – transitional flow, type B (after phase change: force chains created and destroyed);

(iv) $C > C_{\mathrm{qs}}$ – quasi-static flow (force chains persistent).

The flow classification is illustrated in figure 13. This figure is basically a schematic regime chart. It is mostly qualitative, and a much more detailed study would be needed to quantitatively determine curves $C_{\mathrm{r}}(B)$, $C_{\mathrm{pc}}(B)$ and $C_{\mathrm{qs}}(B)$ which separate different regimes. It seems logical that for very small B the value of C_{r} would approach C_{pc}, and there would be no type A transitional flow. This limiting concentration, $C_{\mathrm{r}} = C_{\mathrm{pc}} \equiv C_0$ (for $B \rightarrow 0$) is the theoretical limit of applicability of kinetic theory. Phase-change concentration C_{pc} is probably not very strongly B-dependent, except for rather high B. The quasi-static concentration C_{qs} is probably very close to the dense hexagonal packing concentration $C = 0.907$. However, it is expected to increase as B increases, since for higher B actual particle deformations (overlaps) occupy more space and effectively reduce solid volume fraction.

In figure 14, the contact-number distributions are shown for several cases. Contact number $n_{\mathrm{c}} = 0$ represents free travelling, $n_{\mathrm{c}} = 1$ represents binary contacts, and $n_{\mathrm{c}} > 1$ represent multiple contacts. For $C = 0.8$ and $B = 0.001$, the fraction of multiple contacts is very small, while for $B = 0.01$ it is more significant. By the above classification, the former flow is just barely type A transitional, while the latter is deeply in the type A regime. For $C = 0.85$, for both $B = 0.001$ and $B = 0.01$, flows are type B transitional, just after the phase change. For $C = 0.9$, for both $B = 0.001$ and $B = 0.01$, flows are type B transitional, but close to the quasi-static regime.

In figure 15, the contact-angle distributions are shown for several cases. Strong collisional anisotropy can be observed for $C = 0.8$. In this case the majority of

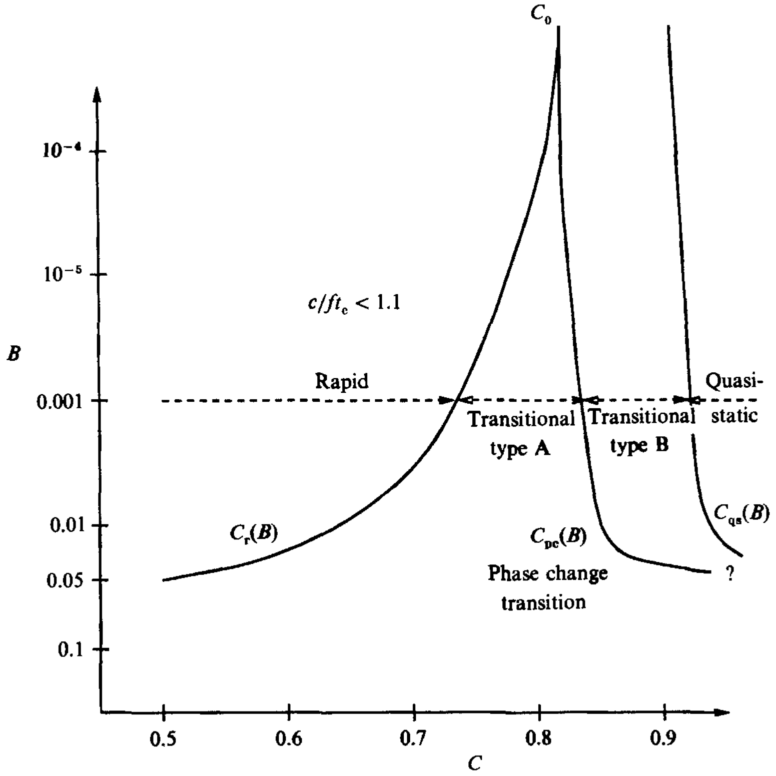

FIGURE 13. Flow classification (schematic regime chart).

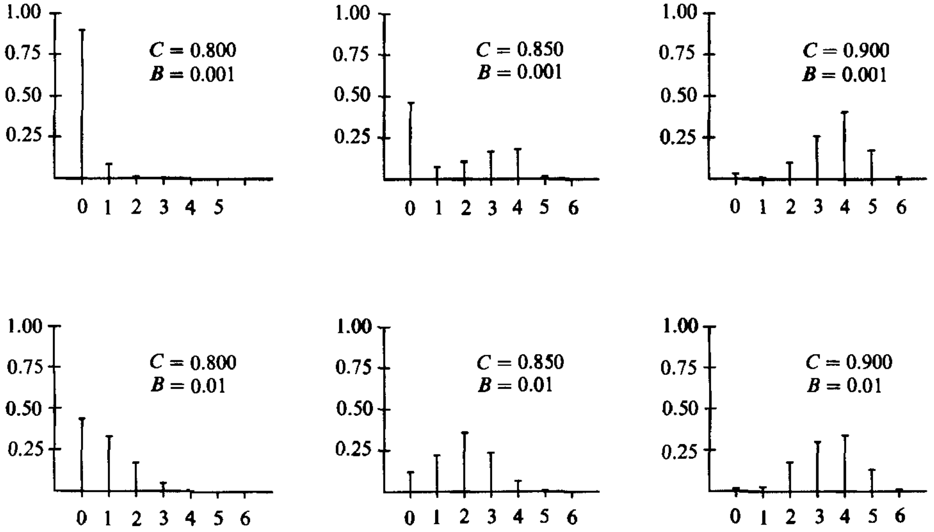

FIGURE 14. Contact-number distributions.

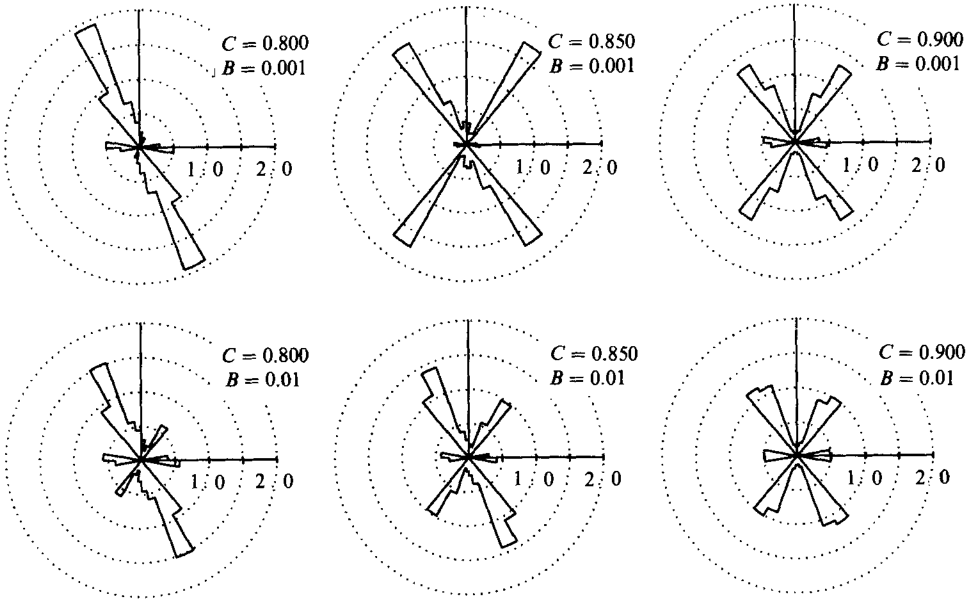

FIGURE 15. Contact-angle distributions.

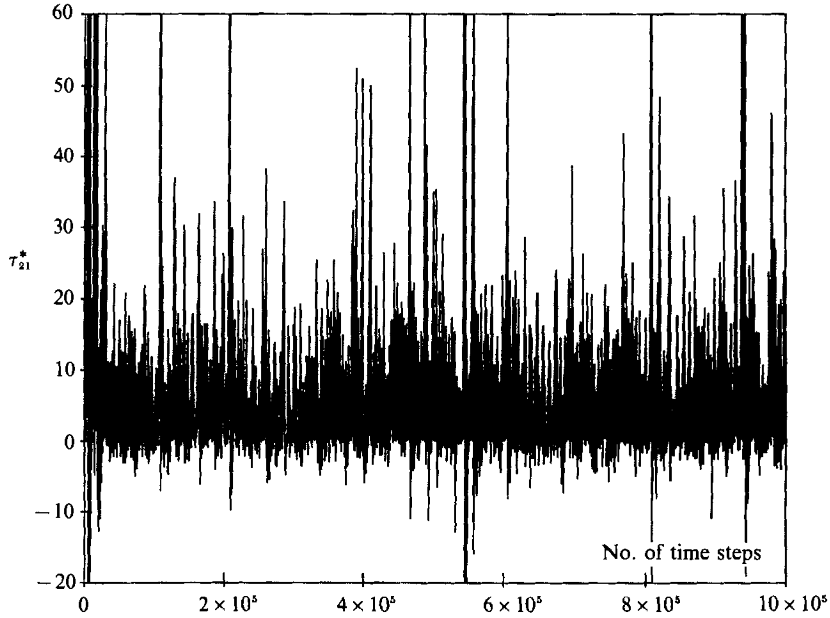

FIGURE 16. Dimensionless shear stress *vs.* time ($C = 0.8$, $B = 0.001$).

contacts are about an angle of 115°. After phase change ($C = 0.85$), force chains are formed in two principal directions corresponding to the hexagonal packing: 60° and 120°. For $C = 0.9$, the majority of contacts are still in directions corresponding to the hexagonal packing, but there is also a significant percentage of angles close to 0°, corresponding to a square-packed region about the rolling layer, as will be shown later.

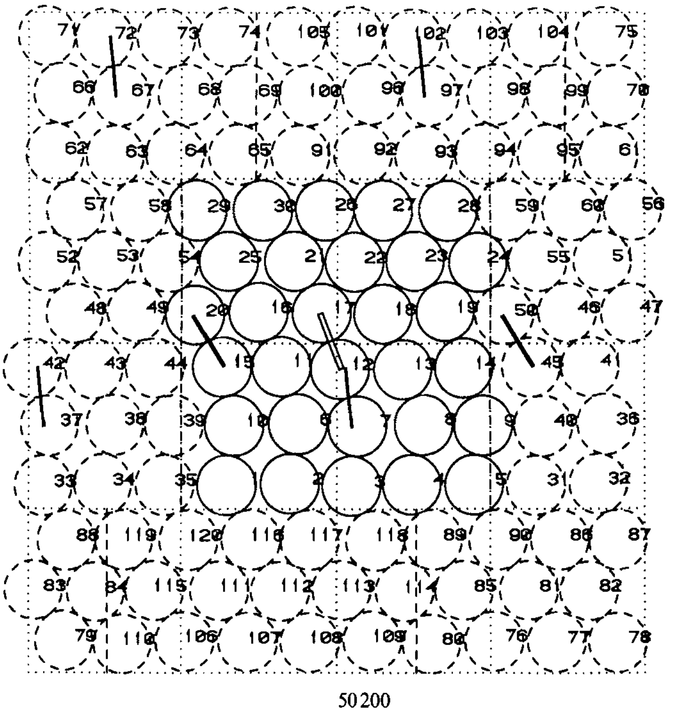

FIGURE 17. Configuration plot ($C = 0.8$, $B = 0.001$) at $nt = 50200$ steps.

To illustrate features of nearly rapid flow (actually type A transitional flow), shear stress development over time is shown for $C = 0.8$, $B = 0.001$ in figure 16. Other stress components show similar variations. This graph shows vigorous fluctuations corresponding to the effect of individual collisions. An instantaneous configuration plot is shown in figure 17. The thickness of rectangles correspond to the magnitude of the forces at contacts. It can be seen that only a few simultaneous contacts (which are actually collisions) exist instantaneously in an assembly. Maximum instantaneous stresses (which extend beyond the frame of figure 16) are up to 200 times higher than the mean value of 7.78. However, these maximum stresses do not correspond to particularly 'strong' collisions, but rather to the formation of temporary, short-lived, force chains extending vertically across the flow cell. These chains, however temporary, have increased the mean value of stresses significantly. Kinetic theory would here underestimate stresses, being unable to predict or describe the formation of these chains. As the concentration increases, these temporary force chains become more frequent and more persistent. Eventually, phase change occurs, after which force chains are present most of the time. However, these chains are being periodically created and destroyed, corresponding to deformations of an assembly.

Some of the most fascinating features of shear flows at high concentrations have been observed for $C = 0.9$, $B = 0.001$. This run is therefore presented in detail. This case falls into the category of nearly quasi-static flow (actually type B transitional flow). The development of stresses in time is shown in figures 18 and 19. These figures reveal remarkable regularity and periodicity. The initial configuration is a regular hexagonal packing. Initially, all of the energy is contained in the translational mode, and there are no contacts between particles. Hence, all contact stress components are

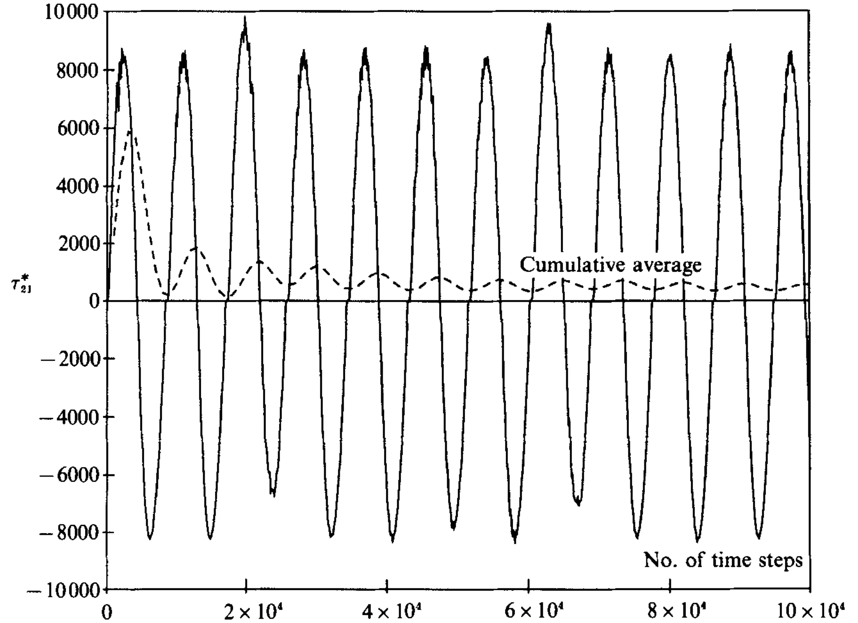

FIGURE 18. Dimensionless shear stress *vs.* time ($C = 0.9$, $B = 0.001$).

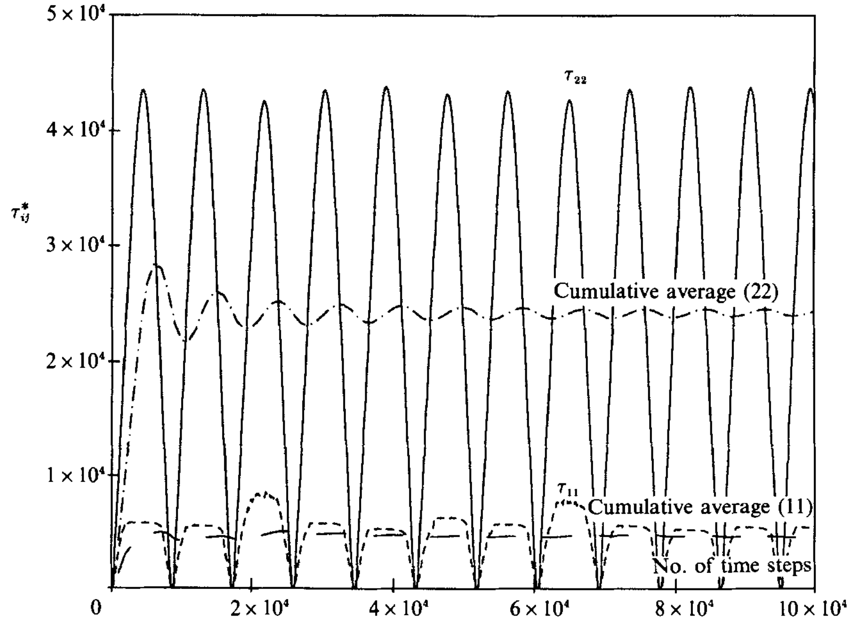

FIGURE 19. Dimensionless normal stresses *vs.* time ($C = 0.9$, $B = 0.001$).

initially zero. The transverse normal stress component τ_{22} increases sharply, reaches a maximum amplitude, and then decreases back to zero within a time period T. The streamwise normal stress component τ_{11} similarly first increases, then reaches a constant-magnitude plateau, and eventually falls off to zero as well. The magnitude of the maximum τ_{11} is much smaller than the maximum τ_{22}. The shear stress reaches a maximum positive value at approximately $\frac{1}{4}T$, passes through zero at $\frac{1}{2}T$ (when

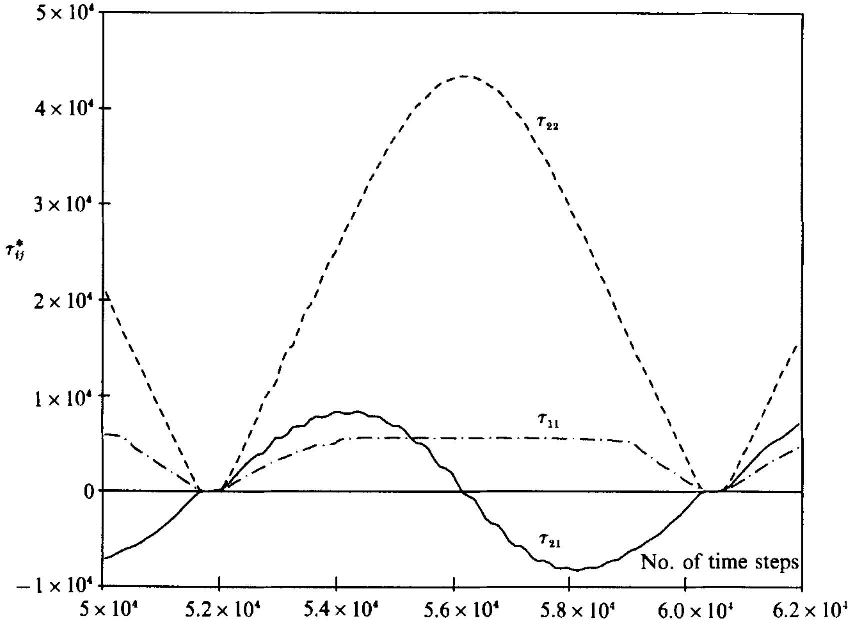

FIGURE 20. Rolling cycle: stresses *vs.* time.

normal stresses are at maximum), changes direction, reaches a maximum negative value at $\frac{3}{4}T$ and goes back to zero after a full period T. The shear stress curve looks very much sinusoidal with period T. At the instant when all contact stress components are nearly zero, the system configuration returns to a hexagonal packing. The whole cycle then repeats itself again and again.

The detailed stress *vs.* time curves are plotted for one cycle in figure 20. Instantaneous configurations at the beginning of the cycle, $\frac{1}{4}T$, $\frac{1}{2}T$ and $\frac{3}{4}T$ are shown in figure 21. In these configuration plots interparticle forces are represented as rectangles centred at the contact point, and inclined in the direction of the actual contact force. The thickness of a rectangle is proportional to the magnitude of the contact force. Dashed lines represent contact forces with a magnitude less than $\frac{1}{10}$ of the maximum force during the sequence. These figures reveal what is actually going on during one period T. It can be seen that the mechanism responsible for the shear flow is a rolling layer (particles 1, 2, 3, 4, 5) formed between two hexagonally packed granular masses moving in opposite directions relative to each other. The period T corresponds to the time period required for one particle (i.e. no. 7) to roll over a particle in the rolling layer (i.e. no. 3). Thus, the period T will be termed 'rolling cycle'. The formation of principal force chains can be observed. In the first quarter of a cycle, the principal force chains are formed, which are inclined at an angle of 120° from the horizontal (x-axis). In the second quarter of a rolling cycle, particles rolling about the rolling layer create rhomboidal packing, in which magnitudes of forces are higher than in hexagonally packed regions. In the same time, the second principal direction is activated (contact angle 60° with the x-axis), but forces in this second chain are smaller than in the first. In these contacts the tangential force component is at the friction limit, which can be seen from the inclination angle of the force with respect to the contact normal. Therefore, the sliding takes place along a plane inclined 120° from the x-axis. During this time, the shear stress reaches a maximum (positive) level. Frictional dissipation of energy is at its maximum as well.

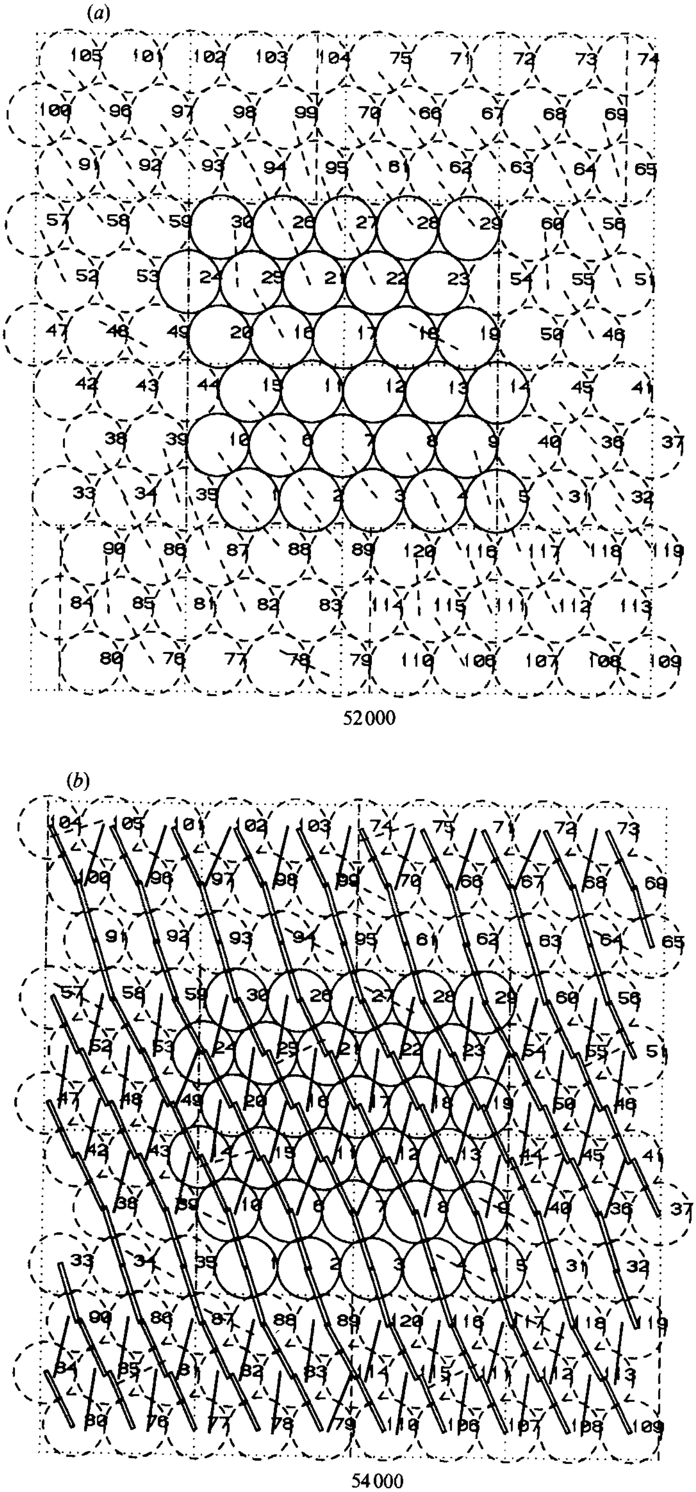

FIGURE 21 (*a*, *b*). For caption see facing page.

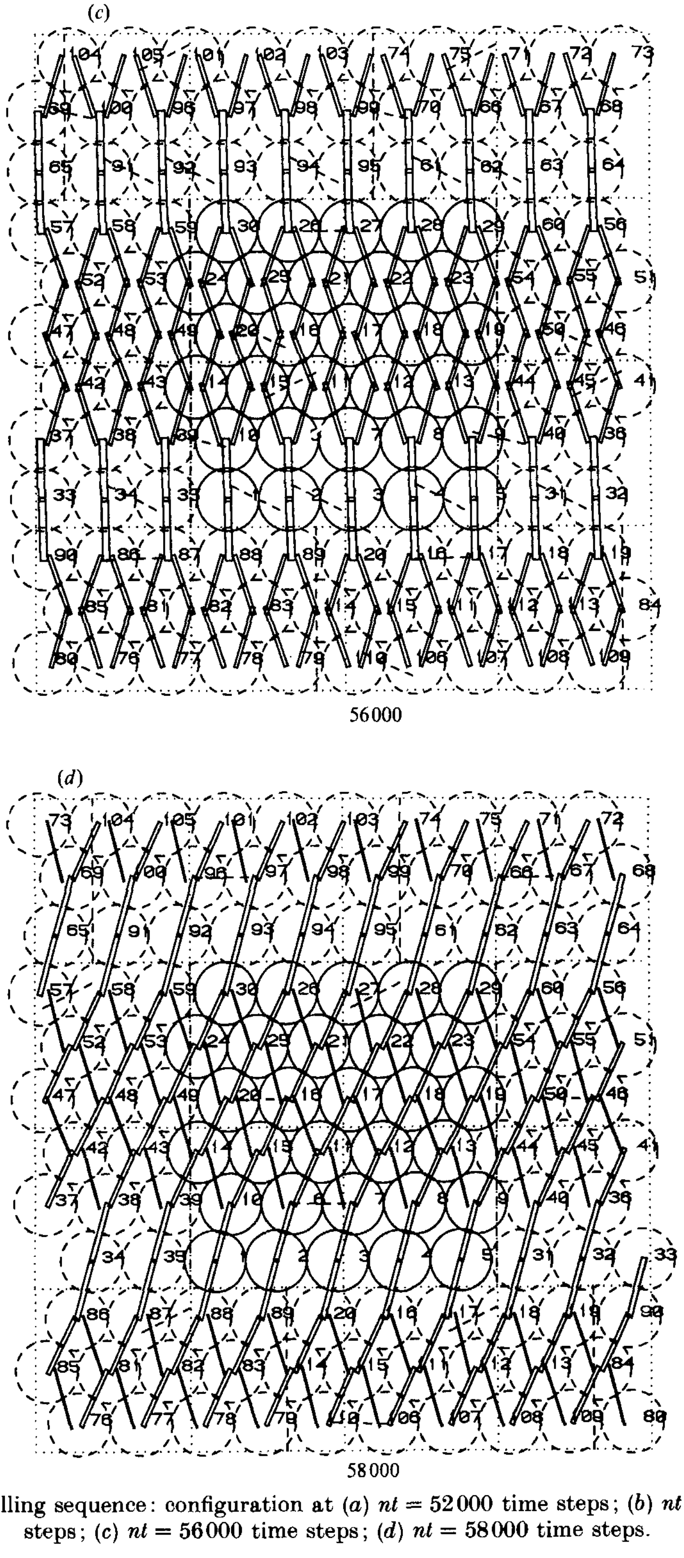

FIGURE 21. Rolling sequence: configuration at (*a*) $nt = 52000$ time steps; (*b*) $nt = 54000$ time steps; (*c*) $nt = 56000$ time steps; (*d*) $nt = 58000$ time steps.

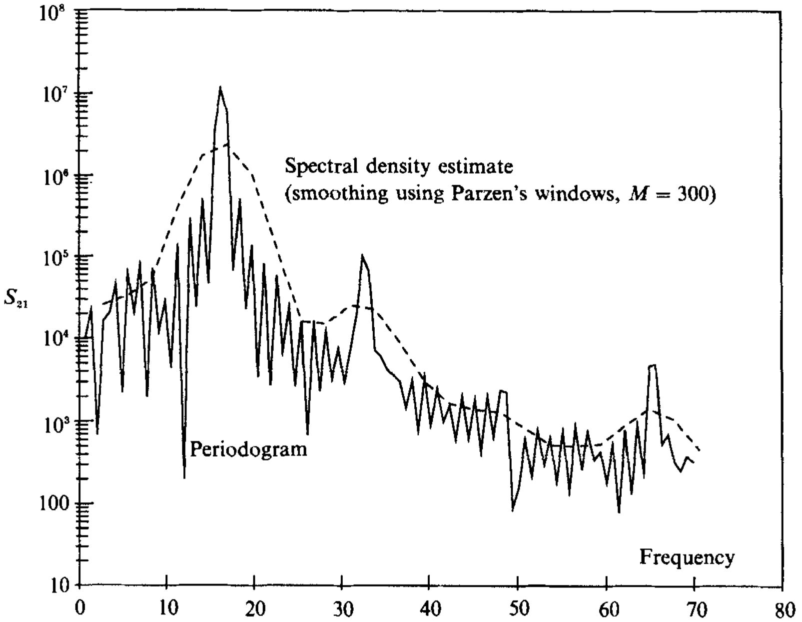

FIGURE 22. Periodogram and spectral density estimate for shear stress time series ($C = 0.9$, $B = 0.001$).

Eventually, the rolling layer and neighbouring rows of particles form a perfectly square packing, which requires more space, and thus compresses the hexagonal portion. The configuration is perfectly symmetric. Forces in two principal chains are equal in magnitude. This instant corresponds to half of the cycle ($\frac{1}{2}T$) when normal stresses are at a maximum, which can be seen from thickness of force rectangles at this instant. At this instant, shear stress passes through zero. As rolling continues, forces in chains decay in magnitude, since square packing deforms into rhomboidal which requires less space. Force chains at 60° angle are now stronger, and sliding takes place at contacts at 120°. Shear stress reverses direction. Eventually, in the last quarter of the rolling cycle, the whole assembly relaxes towards uniform hexagonal packing and all stress components decrease to zero. At the end of the cycle, potential energy is nearly zero, but kinetic energy reaches a maximum, and this is responsible for the start of the next cycle. This is a complete description of one rolling cycle.

The period of the rolling cycle T can be measured from simulation results. Spectral analysis of the time series τ_{21} was performed using IMSL software routines PFFT and SSWB. Results are shown in figure 22. In this figure, the fluctuating line is a periodogram of the time series, obtained by routine PFFT. The smooth curve is a spectral energy density estimate obtained by routine SSWD which uses Parzen's window with parameter $M = 300$. The dominant frequency is equal to $16.3\dot{\gamma}$, from which it turns out that $T = 0.383/\dot{\gamma}$, or about 8600 time steps. The period T can also be estimated using simple arguments. Let v be the horizontal velocity of hexagonal 'blocks' moving in opposite directions about a rolling layer. Periodic boundary conditions impose at least one rolling layer in each layer of cells. It was observed that there was only one rolling layer in a cell, such that distance between two rolling layers (original and cloned) is equal to b, the height of the calculation cell. In order to maintain a specified shear rate $\dot{\gamma}$ and assuming that blocks move with constant relative velocity $2v$, it follows that $v = \frac{1}{2}\dot{\gamma}b$. Since each particle in the block has to travel a horizontal distance D during one cycle, the period of rolling is $T \approx D/v = 2D/\dot{\gamma}b$. For $C = 0.9$, one obtains $T \approx 0.384$, which is almost identical to the measured value.

In the detailed presentation of this run it was demonstrated that the mechanism of shear flow at high concentrations is the rolling of particles about the rolling layer. The rolling cycle is repeated periodically, and its period can be accurately estimated using simple arguments. During the rolling cycle stress components behave very regularly, and it is believed that the problem should be tractable analytically. Therefore, an interesting and challenging problem is posed here: to theoretically describe stress variations during the rolling cycle utilizing presented microscopic informations. The time-averaged (mean) stresses would then be easily obtained. The analytical solution of this problem would be of great importance for the description of the granular material behaviour near the quasi-static limit.

4. Conclusions

In this study, a numerical model is utilized to directly simulate the mechanical behaviour of a small assembly of uniform, inelastic, frictional, deformable disks in a simple shear flow. The study is focused on high solids concentrations, up to $C = 0.9$, in order to capture and explain the transition between rapid and quasi-static granular flows. In a simple shear flow, with an assumed viscoelastic, frictional contact force model, the dimensionless stresses $\tau^*_{ij} = \tau_{ij}/(\rho_s D^2 \dot{\gamma}^2)$ are a function of concentration C, the parameter $B = \dot{\gamma}/(K_n/m)^{\frac{1}{2}}$ (dimensionless shear rate), and material constants). The range of B from 0.001 to 0.0707 was investigated for C ranging from 0.5 to 0.9. Larger values of B correspond to faster flow at a constant contact stiffness, or, equivalently, softer particles at a constant shear rate. It is found that τ^*_{ij} is nearly independent of B for $C < 0.75$, but as the concentration increases, τ^*_{ij} decreases as B increases. Phenomenological forms of constitutive equations are derived as $\tau^*_{ij} = a_{ij}(C) B^{-n_{ij}(C)}$, based on the simulation results. The values of n_{ij}, estimated by regression analysis, are found to range from nearly zero for $C = 0.775$ (corresponding to square power dependency of dimensional stresses on shear rate in the rapid regime) to nearly two for $C = 0.9$ (corresponding to shear-rate independence in the quasi-static regime). The intermediate range of concentration corresponds to the transition between these regimes.

The phase-change type of transition was clearly observed between $C = 0.825$ and 0.85 for both $B = 0.001$ and $B = 0.01$. For $B = 0.0707$, the phase change transition did not occur. In general, the phase-change concentration C_{pc} is a function of B, and is expected to slightly decrease as B decreases. Transitional flows are classified into two types: type A, prior to phase change; and type B, after phase change. Mechanisms governing transitional flows are observed and discussed. Type A transitional flow is similar to rapid flow, i.e. mostly collisional. However, short-lived force chains occasionally appear and increase the value of time-averaged stresses. As concentration increases, these temporary force chains become more frequent and more persistent. After the phase change, in the type B transitional regime, force chains are periodically created and destroyed corresponding to deformations of the assembly. The shear flow is maintained by rolling mechanism about a rolling layer. Eventually, if concentration were increased beyond the close-packed density, the system would reach the quasi-static limit.

The particular run for $C = 0.9$, $B = 0.001$ (near the quasi-static limit) is presented in detail to illustrate the remarkable regularity and periodicity observed when following the stress development over time. Stresses were found to oscillate with a frequency corresponding to the period of rolling of one particle over another (rolling cycle). A theoretical treatment of this problem seems feasible with the aid of information provided by this study. The analytical solution of this problem would be of great importance, because in that case the effect of material parameters and the effect of the number of particles would not have to be sought by time-consuming sets of numerical experiments as in the present study.

The sensitivity of observed behaviour at high concentrations to a slight perturbation of particle diameters in the uniform size distribution should be investigated. In this case perfectly regular structural patterns may not develop. Since mixing of particles of similar sizes at high concentrations is unlikely, the effect of initial conditions would probably be significant. The material behaviour could be only predicted in a mean sense, taking an average over many runs with different initial conditions.

As discussed earlier, the effect of sample size (the number of particles N) is probably very important, especially at high concentrations (type B transitional regime). The sample-size effects may require different parametrization in cases of uniform shearing and local shearing (the rolling layer). Magnitudes of stresses and phenomenological constitutive equations would probably be affected. However, it is believed that the power-law trend discovered in the relationship between dimensionless stresses and an apparent shear rate (with powers descending from 2 towards 0 as concentration increases) would still be valid. This result is considered to be the most important result of the study.

Investigation of the sample size effects by repeating the analysis with a larger number of particles (for instance, 120 and 480) as well as the investigation of the effect of material parameters remains for future study.

This study is supported by the US Army Cold Regions Research and Engineering Laboratory through Contract No. DACA89-87-K-0001.

Appendix A. Derivation of the energy equation

In this Appendix the instantaneous mechanical-energy equation for the control volume (primary cell) is derived using a microscopic approach. The derivation yields expressions for translational and rotational kinetic energy, potential energy, rate of energy dissipation and the stress tensor in forms suitable for numerical evaluation.

Newton's equation for the translational motion of particle p is

$$m\ddot{\boldsymbol{x}}_p = \sum_{c=1}^{M_p} \boldsymbol{F}_{pq_c}, \tag{A 1}$$

where $\boldsymbol{x}_p$ is the position vector of the centre of particle p, $\boldsymbol{F}_{pq_c}$ is the total force exerted by particle q_c on particle p at contact c, M_p is the number of contacts of particle p, and m is the mass of a particle. Multiplying equation (A 1) by $\dot{\boldsymbol{x}}_p$ and summing the resulting equations for all particles yields

$$\frac{\mathrm{d}}{\mathrm{d}t}\sum_{p=1}^{N}[\tfrac{1}{2}m\dot{\boldsymbol{x}}_p^2] = \sum_{p=1}^{N}\sum_{c=1}^{M_p}[\boldsymbol{F}_{pq_c}\cdot\dot{\boldsymbol{x}}_p]. \tag{A 2}$$

In order to evaluate the term on the right-hand side, two types of contacts are considered (figure 23). If both particles which are involved in a contact are interior,

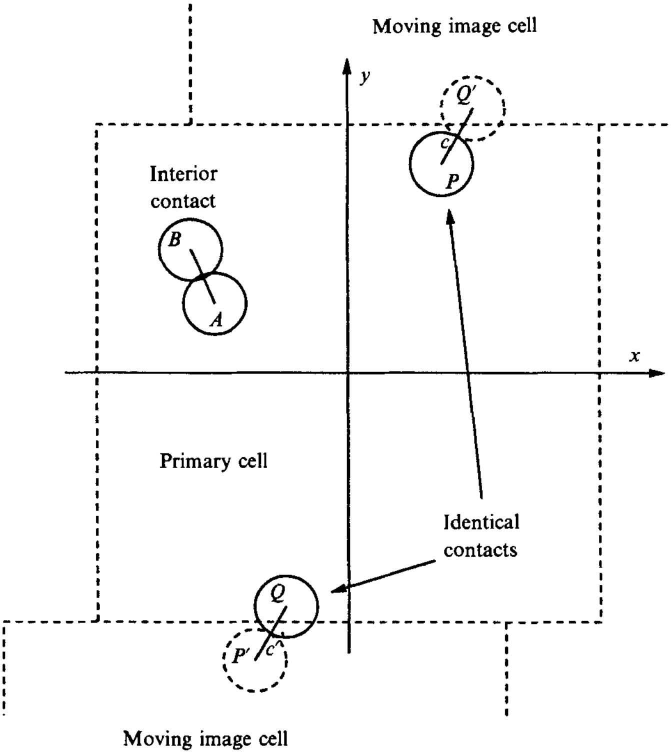

FIGURE 23. Interior and boundary contacts in simple shear flow.

such as particles A and B, then the total contribution to the right-hand side of (A 2) due to this contact is

$$\boldsymbol{F}_{AB}\cdot\dot{\boldsymbol{x}}_A+\boldsymbol{F}_{BA}\cdot\dot{\boldsymbol{x}}_B=\boldsymbol{F}_{AB}\cdot\dot{\boldsymbol{x}}_{AB},\tag{A 3}$$

where $\dot{\boldsymbol{x}}_{AB}=\dot{\boldsymbol{x}}_A-\dot{\boldsymbol{x}}_B$ is the relative velocity of particles A and B. If a contact is between an interior and exterior particle, such as particles P and Q', then because of periodic boundaries there is also a contact between particle Q (a clone of Q') and particle P' (which is a clone of P). These two contacts are really identical, since the relative position and velocity of particles P and Q' are exactly the same as those of P' and Q. The total contribution to the right-hand side of (A 2) of these two identical boundary contacts is

$$\boldsymbol{F}_{PQ'}\cdot\dot{\boldsymbol{x}}_P+\boldsymbol{F}_{QP'}\cdot\dot{\boldsymbol{x}}_Q=\boldsymbol{F}_{PQ'}\cdot(\dot{\boldsymbol{x}}_P-\dot{\boldsymbol{x}}_Q)=\boldsymbol{F}_{PQ'}\cdot\dot{\boldsymbol{x}}_{PQ'}+\boldsymbol{F}_{PQ'}\cdot\dot{\boldsymbol{x}}_{Q'Q}.\tag{A 4}$$

Note that only the contact between P and Q' is actually within the cell. In (A 4) $\dot{\boldsymbol{x}}_{Q'Q}=\dot{\boldsymbol{x}}_{Q'}-\dot{\boldsymbol{x}}_Q$ is the relative velocity of clone Q' with respect to its original Q. This relative velocity is induced by the shear field, and can be expressed as

$$\dot{\boldsymbol{x}}_{Q'Q}=\boldsymbol{D}\cdot(\boldsymbol{x}_{Q'}-\boldsymbol{x}_Q),\tag{A 5}$$

where the Cartesian components of $\boldsymbol{D}$ are $D_{12}=\dot{\gamma}$, $D_{11}=D_{22}=D_{21}=0$. Note that $\boldsymbol{x}_{Q'}-\boldsymbol{x}_Q=\boldsymbol{x}_c-\boldsymbol{x}_{c'}$, where $\boldsymbol{x}_c$ and $\boldsymbol{x}_{c'}$ are position vectors of contact points C (between P and Q') and C' (between Q and P'). Using $\boldsymbol{F}_{PQ'}=\boldsymbol{F}_{P'Q}=-\boldsymbol{F}_{QP'}$, it therefore follows that

$$\boldsymbol{F}_{PQ'}\cdot\dot{\boldsymbol{x}}_{Q'Q}=\boldsymbol{F}_{PQ'}\cdot[\boldsymbol{D}\cdot(\boldsymbol{x}_c-\boldsymbol{x}_{c'})]=\boldsymbol{F}_{PQ'}\cdot(\boldsymbol{D}\cdot\boldsymbol{x}_c)+\boldsymbol{F}_{QP'}\cdot(\boldsymbol{D}\cdot\boldsymbol{x}_{c'}).\tag{A 6}$$

Using (A 3), (A 4) and (A 5), equation (A 2) can be written as

$$\frac{\mathrm{d}}{\mathrm{d}t}\sum_{p=1}^{N}[\tfrac{1}{2}m\dot{\boldsymbol{x}}_p^2] = \sum_{p=1}^{N}\sum_{c=1}^{M_p}[\boldsymbol{F}_{pq_c}\cdot\dot{\boldsymbol{x}}_p] = \sum_{c=1}^{M}[\boldsymbol{F}_c\cdot\dot{\boldsymbol{x}}_c]+\sum_{B}[\boldsymbol{F}_{pq'}\cdot(\boldsymbol{D}\cdot\boldsymbol{x}_c)]. \qquad \text{(A 7)}$$

In the first term on the right-hand side of (A 7) $\boldsymbol{F}_c$ and $\dot{\boldsymbol{x}}_c$ are the force and relative velocity between particle p and the nearest image of particle q involved in contact c, respectively. Summations in this term include all contacts within a cell, counting each contact only once. In the second term on the right-hand side of (A 7) $\boldsymbol{F}_{pq'}$ and $\boldsymbol{x}_c$ are force and position vectors of the contact point between interior particle p and exterior particle q' (image of q). The summation in this term goes over all boundary contacts, including both (identical) contacts such as c and c'. Using abbreviations $\boldsymbol{F}^c \equiv \boldsymbol{F}_{pq}$ and $\dot{\boldsymbol{x}}_c \equiv \dot{\boldsymbol{x}}_{pq} = \dot{\boldsymbol{x}}_p - \dot{\boldsymbol{x}}_q$, $\dot{\boldsymbol{x}}^p \equiv \dot{\boldsymbol{x}}_p$, and switching to standard indicial notation (A 7) can be written as

$$\frac{\mathrm{d}}{\mathrm{d}t}\sum_{p=1}^{N}[\tfrac{1}{2}m\dot{x}_i^p\dot{x}_i^p] = \sum_{c=1}^{M}[F_i^c\dot{x}_i^c]+D_{ij}\sum_{c=1}^{M_B}[F_i^c x_j^c], \qquad \text{(A 8)}$$

where M is the total number of contacts within a cell and M_B is the total number of boundary contacts between one interior and one exterior particle. The above equation expresses the time rate of change of total translational kinetic energy in a cell. The next step is to separate kinetic energy due to mean shear flow and fluctuating motion of particles about the mean. The velocity of particle p can be separated into mean and fluctuating components as

$$\dot{x}_i^p \equiv u_i^p = D_{ij}x_j^p + u_i'^p. \qquad \text{(A 9)}$$

The rate of change of kinetic energy of particle p is then

$$\begin{aligned}\frac{1}{2}\frac{\mathrm{d}}{\mathrm{d}t}(u_i^p u_i^p) = u_i^p\dot{u}_i^p &= (u_i'^p + D_{ij}x_j^p)(\dot{u}_i'^p + D_{ik}u_k^p) = u_i'^p\dot{u}_i'^p + D_{ik}u_i'^p u_k^p + D_{ij}x_j^p\dot{u}_i^p \\ &= \frac{1}{2}\frac{\mathrm{d}}{\mathrm{d}t}(u_i'^p u_i'^p) + D_{ij}x_j^p\dot{u}_i^p + D_{ik}u_i'^p u_k'^p + D_{ik}D_{kl}u_i'^p x_k^p. \qquad \text{(A 10)}\end{aligned}$$

But, $D_{ik}D_{kl} = 0$ for simple shear flow. Hence, (A 8) becomes

$$\frac{1}{2}\frac{\mathrm{d}}{\mathrm{d}t}\sum_{p=1}^{N}[mu_i'^p u_i'^p] = \sum_{c=1}^{M}[F_i^c\dot{x}_i^c]+D_{ij}\left\{\sum_{c=1}^{M_B}[F_i^c x_j^c]-\sum_{p=1}^{N}[mu_i'^p u_j'^p + mx_j^p\dot{u}_i^p]\right\}. \qquad \text{(A 11)}$$

This equation expresses the time rate of change of fluctuation translational energy (temperature).

The rotational contribution to the energy equation is considered next. Newton's equation for rotational motion of particle p is

$$I\ddot{\theta}_p = \sum_{c=1}^{M_p}[\boldsymbol{r}_{cp}\times\boldsymbol{F}_{pq_c}]_z, \qquad \text{(A 12)}$$

where $\dot{\theta}_p$ is the angular velocity of particle p, $\boldsymbol{r}_{cp}$ is the position vector of contact point c with respect to the centre of particle p, and I is particle's moment of inertia. Multiplying (A 12) by $\dot{\theta}_p$ and summing the resulting equations for all particles yields

$$\frac{\mathrm{d}}{\mathrm{d}t}\sum_{p=1}^{N}[\tfrac{1}{2}I\dot{\theta}_p^2] = \sum_{p=1}^{N}\sum_{c=1}^{M_p}[\boldsymbol{r}_{cp}\times\boldsymbol{F}_{pq_c}]_z\,\dot{\theta}_p. \qquad \text{(A 13)}$$

The total contribution of a contact (i.e. between particles A and B) to the right-hand side of the above equation is

$$[\boldsymbol{r}_{CA} \times \boldsymbol{F}_{AB}]_z \dot{\theta}_A + [\boldsymbol{r}_{CB} \times \boldsymbol{F}_{BA}]_z \dot{\theta}_B = [\boldsymbol{r}_{CA} \times \boldsymbol{F}_{AB}]_z \dot{\theta}_{AB}, \tag{A 14}$$

where $\dot{\theta}_{AB} = \dot{\theta}_A + \dot{\theta}_B$ is the relative angular velocity of particles A and B. Therefore,

$$\frac{\mathrm{d}}{\mathrm{d}t} \sum_{p=1}^{N} [\tfrac{1}{2} I \dot{\theta}_p^2] = \sum_{c=1}^{M} [\boldsymbol{r}^c \times \boldsymbol{F}^c]_z \dot{\theta}_c, \tag{A 15}$$

where $\boldsymbol{r}^c \equiv \boldsymbol{r}_{cp}$, $\boldsymbol{F}^c \equiv \boldsymbol{F}_{pq_c}$, $\dot{\theta}_c \equiv \dot{\theta}_{pq_c} = \dot{\theta}_p + \dot{\theta}_{q_c}$.

The total contact force $\boldsymbol{F}^c$ at contact c consists of normal and tangential components:

$$\boldsymbol{F}^c = -(F_n^c \boldsymbol{k} + F_s^c \boldsymbol{t}), \tag{A 16}$$

where $\boldsymbol{k}$ and $\boldsymbol{t}$ are unit vectors in normal and tangential directions, respectively. The relative velocity $\dot{\boldsymbol{x}}^c$ can be expressed in this coordinate system as

$$\dot{\boldsymbol{x}}^c = \dot{n} \boldsymbol{k} + \dot{s} \boldsymbol{t}, \tag{A 17}$$

where $\dot{n} = \dot{\boldsymbol{x}}^c \cdot \boldsymbol{k}$ and $\dot{s} = \dot{\boldsymbol{x}}^c \cdot \boldsymbol{t}$. Furthermore, $\boldsymbol{r}^c = R\boldsymbol{k}$, and therefore $[\boldsymbol{r}^c \times \boldsymbol{F}^c]_z = -RF_s^c$, where R is particle's radius. Substituting these results into (A 11) and (A 15), one obtains

$$\frac{\mathrm{d}}{\mathrm{d}t} \sum_{p=1}^{N} [\tfrac{1}{2} m u_p'^2] + \sum_{c=1}^{M} [F_n^c \dot{n} + F_s \dot{s}] = D_{ij} \left\{ \sum_{c=1}^{M_B} [F_i^c x_j^c] - \sum_{p=1}^{N} [m u_i'^p u_j'^p + m x_j^p \dot{u}_i^p] \right\}, \tag{A 18}$$

$$\frac{\mathrm{d}}{\mathrm{d}t} \sum_{p=1}^{N} [\tfrac{1}{2} I \dot{\theta}_p^2] + \sum_{c=1}^{M} F_s^c R \dot{\theta}_c = 0. \tag{A 19}$$

Adding (A 18) and (A 19), one obtains

$$\frac{1}{2} \frac{\mathrm{d}}{\mathrm{d}t} \sum_{p=1}^{N} [m u_p'^2 + I \dot{\theta}_p^2] + \sum_{c=1}^{M} [F_n^c \dot{n} + F_s^c \dot{q}] = D_{ij} \left\{ \sum_{c=1}^{M_B} [F_i^c x_j^c] - \sum_{p=1}^{N} [m u_i'^p u_j'^p + m x_j^p \dot{u}_i^p] \right\}, \tag{A 20}$$

where $\dot{q} = \dot{s} + R\dot{\theta}_c$ is the relative tangential velocity at the contact.

The above equation expresses the instantaneous energy balance in a cell. A more detailed form is obtained if the actual contact force model is specified. In this study, the viscoelastic force model described in §2 is used. In this model, the normal component of the contact force consists of spring and dashpot contributions:

$$F_n = K_n n + C_n \dot{n}. \tag{A 21}$$

The tangential component is given by:

$$F_s = \min(|K_s q + C_s \dot{q}|; \mu K_n n) \operatorname{sign}(\dot{q}). \tag{A 22}$$

Hence, (A 20) becomes

$$\begin{aligned} &\frac{1}{2} \frac{\mathrm{d}}{\mathrm{d}t} \left\{ \sum_{p=1}^{N} [m u_p'^2 + I \dot{\theta}_p^2] + \sum_{c=1}^{M} [K_n n^2] + \sum_{c=1}^{M_1} [K_s q^2] \right\} \\ &\quad = D_{ij} \left\{ \sum_{c=1}^{M_B} [F_i^c x_j^c] - \sum_{p=1}^{N} m [u_i'^p u_j'^p + x_j^p \dot{u}_i^p] \right\} - \left\{ \sum_{c=1}^{M} [C_n \dot{n}^2] + \sum_{c=1}^{M_1} [C_s \dot{q}^2] + \sum_{c=M_1}^{M_2} [\mu K_n n |\dot{q}|] \right\}, \end{aligned} \tag{A 23}$$

where M_1 is the number of non-sliding contacts and M_2 is the number of sliding contacts.

The above equation can be written as

$$\frac{\mathrm{d}}{\mathrm{d}t}(T+V) = \tau_{ji} D_{ij} - \Gamma, \tag{A 24}$$

where a physical interpretation of terms is as follows: $T =$ kinetic energy per unit volume, $V =$ potential energy per unit volume, $\Gamma =$ rate of energy dissipation per unit volume, $\tau_{ij} = \tau^{\mathrm{k}}_{ij} + \tau^{c}_{ij} =$ stress tensor. These terms are given by

$$T = \frac{1}{A} \sum_{p=1}^{N} \tfrac{1}{2}[m u_p'^2 + I \dot{\theta}_p^2], \tag{A 25}$$

$$V = \frac{1}{A} \left\{ \sum_{c=1}^{M} \tfrac{1}{2}[K_n n^2] + \sum_{c=1}^{M_1} \tfrac{1}{2}[K_s q^2] \right\}, \tag{A 26}$$

$$\Gamma = \frac{1}{A} \left\{ \sum_{c=1}^{M} [C_n \dot{n}^2] + \sum_{c=1}^{M_1} [C_s \dot{q}^2] + \sum_{c=1}^{M_2} [\mu K_n n |\dot{q}|] \right\}, \tag{A 27}$$

$$\tau^{\mathrm{k}}_{ij} = -\frac{1}{A} \sum_{p=1}^{N} m(u_i'^p u_j'^p), \tag{A 28}$$

$$\tau^{c}_{ij} = \frac{1}{A} \sum_{c=1}^{M_B} [x_i^c F_j^c] - \sum_{p=1}^{N} m[x_i^p \dot{u}_j^p] \tag{A 29}$$

where A is area of the cell.

It can be seen that the energy equation contains three major terms: rate of change of total energy, rate of energy dissipation and rate of work done by stress (stress power). The stress tensor consists of two terms, kinetic stress τ^{k}_{ij} and contact stress τ^{c}_{ij}. All of these terms are explicitly expressed in forms suitable for numerical evaluation. However, a little bit more work is needed to reduce the contact stress tensor given by (A 29) into a more suitable form. Note that interior contacts can be trivially added to summation over boundary contacts in the first term of (A 29), since $x_i^c F_j^{pq_c} = -x_i^c F_j^{q_c p}$. Using $x_i^c = x_i^p + r_i^{cp}$, the first term in (A 29) can be written as

$$\sum_{c=1}^{M_B} [x_i^c F_j^c] = \sum_{p=1}^{N} \sum_{c=1}^{M_p} x_i^c F_j^{pq_c} = \sum_{p=1}^{N} \sum_{c=1}^{M_p} r_i^{cp} F_j^{pq_c} + \sum_{p=1}^{N} x_i^p \sum_{c=1}^{M_p} F_j^{pq_c}. \tag{A 30}$$

Substituting this result back into (A 29), cancelling acceleration terms and noting that $r_i^{cp} = -r_i^{cq_c}$ and $F_j^{pq_c} = -F_j^{q_c p}$, one finally obtains

$$\tau^{c}_{ij} = \frac{1}{A} \sum_{p=1}^{N} \sum_{c=1}^{M_p} r_i^{cp} F_j^{pq_c} = \frac{D}{A} \sum_{c=1}^{M} k_i^c F_j^c, \tag{A 31}$$

where $Dk_i^c = r_i^{cp} - r_i^{cq}$ is the 'branch vector' from the centre of particle p to the centre of particle q, and F_j^c is contact force exerted from particle q on particle p at contact c.

There is more merit in this derivation than merely obtaining the spatially averaged terms involved in the energy balance. The derivation yields a form of the contact stress tensor given by (A 31) that is identical to the expression derived by Cundall *et al.* (1982) but by using different arguments. However, they assumed that inertia forces are negligible throughout the derivation, having in mind application to quasi-static problems only. Several other researchers (Drecher & de Josselin de Jong 1972; Christofferson, Mehrabadi & Nemat Nasser 1981) have arrived at the same result using the principle of virtual work, but they all neglected inertia terms as well. Therefore, it was not apparent that equation (A 31) could be used for all situations, including dynamic (rapid flow) and quasi-static problems. This dilemma is now resolved, since it was shown that certain inertia-related terms do get cancelled and need not be neglected directly. One may think of this derivation as an application of the real work principle, instead of virtual. It should be noted that the same equation (A 31) was used by Walton & Braun (1985) in their simple shear flow simulation in the dynamic regime, but they have not presented any derivation.

One final point is that the contact stress tensor given by (A 31) can be reduced to a collisional stress tensor obtained by the kinetic theory of rapid granular flows, assuming that contacts between particles are binary. This assumption is valid for low to moderately high concentrations and stiff particles (rigid-particle limit corresponds to $K_n \rightarrow \infty$). These arguments are presented in more details in Babić (1989).

Appendix B. Summary of results

This Appendix contains a summary of the simulation results in tabulated form. Tables 1–3 contain a summary of results for $B = 0.001$, 0.01 and 0.0707, respectively. All results in this table are cumulative time averages of instantaneous space-averaged quantities. An asterisk denotes a dimensionless quantity scaled by the factor given in the table below. The definition of terms in the tables is as follows:

Symbol	Quantity	Defined by equation	Scaled by
τ_{ij}	Stress tensor	(14) + (15)	$\rho_s D^2 \dot{\gamma}^2$
T_t	Transl. kinetic energy	(10)	$\rho_s D^2 \dot{\gamma}^2$
T_r	Rotat. kinetic energy	(11)	$\rho_s D^2 \dot{\gamma}^2$
V	Potential energy	(12)	$\rho_s D^2 \dot{\gamma}^2$
Γ	Total rate of ener. dissip.	(13)	$\rho_s D^2 \dot{\gamma}^3$
Γ_{nd}	Γ due to normal damping	1st term in (13)	$\rho_s D^2 \dot{\gamma}^3$
Γ_{fr}	Γ due to friction	3rd term in (13)	$\rho_s D^2 \dot{\gamma}^3$
Ω	Mean angular velocity	$\dot{\theta}_p$	$-\dot{\gamma}$
c	Coordination number	$\frac{2M}{N}$	
f	Frequency of collisions		
E_{ij}	Fabric tensor	$\overline{k_i k_j}$	
β_s	Fraction of slipping contacts		

C	0.500	0.600	0.700	0.750	0.775	0.800	0.825	0.850	0.875	0.900
τ^*_{21}	0.73	1.39	2.57	3.25	5.51	7.78	14.35	97.81	198.36	304.00
τ^*_{11}	1.40	2.58	4.54	4.46	6.79	9.53	15.33	461.85	2325	4501
τ^*_{22}	1.31	2.42	5.59	9.57	18.50	25.56	45.90	2172.10	12 370	24 275
T^*_t	0.095	0.115	0.114	0.218	0.338	0.560	0.635	0.774	0.896	0.711
T^*_r	0.072	0.093	0.102	0.101	0.132	0.192	0.223	0.697	0.901	0.414
T^*	0.167	0.208	0.216	0.319	0.470	0.752	0.858	1.471	1.797	1.125
V^*	0.001	0.002	0.004	0.006	0.015	0.025	0.156	8.32	147.00	472.32
V/T	0.007	0.010	0.019	0.019	0.032	0.033	0.18	5.65	81.70	420.21
Γ^*_{nd}	0.42	0.79	1.38	1.70	2.67	3.66	5.12	22.21	40.10	32.16
Γ^*_{fr}	0.33	0.65	1.30	1.67	2.99	4.30	9.41	75.40	157.59	264.42
Γ^*	0.75	1.44	2.68	3.37	5.66	7.96	14.53	97.61	197.69	296.58
Ω^*	0.545	0.501	0.573	0.694	0.726	0.745	0.775	0.810	0.820	0.836
c	0.013	0.025	0.058	0.076	0.111	0.130	0.141	1.572	2.69	3.57
f	5.90	11.56	25.56	31.54	41.87	47.25	52.49	66.00	48.65	64.93
$c/(ft_c)$	0.978	0.986	1.023	1.082	1.195	1.237	1.207	10.07	24.85	24.71
E_{11}	0.50	0.51	0.47	0.35	0.30	0.30	0.30	0.26	0.29	0.34
E_{22}	0.50	0.49	0.53	0.65	0.70	0.70	0.70	0.74	0.71	0.66
E_{21}	−0.18	−0.20	−0.18	−0.17	−0.16	−0.17	−0.17	−0.04	−0.02	−0.01
β_s	0.477	0.478	0.491	0.475	0.438	0.412	0.40	0.124	0.076	0.118
$NT/10^3$	1000	1000	2000	2000	2000	2000	500	1000	500	500

TABLE 1. Summary of results for $B = 0.001$ (cumulative time averages)

C	0.500	0.600	0.700	0.750	0.775	0.800	0.825	0.850	0.875	0.900
τ_{21}^*	0.78	1.33	2.80	4.07	4.07	4.58	4.24	13.85	23.64	8.95
τ_{11}^*	1.54	2.54	5.46	7.36	5.69	6.27	5.87	18.16	44.09	56.64
τ_{22}^*	1.33	2.41	6.06	11.34	14.16	16.16	13.41	63.43	159.00	236.84
T_t^*	0.108	0.123	0.146	0.228	0.299	0.488	0.574	0.587	0.989	0.702
T_r^*	0.085	0.104	0.125	0.135	0.137	0.168	0.194	0.478	0.456	0.267
T^*	0.193	0.227	0.271	0.363	0.436	0.656	0.768	1.065	1.445	0.969
V^*	0.013	0.022	0.059	0.110	0.109	0.112	0.088	0.719	2.990	4.973
V/T	0.067	0.098	0.217	0.303	0.249	0.170	0.115	0.675	2.061	5.133
Γ_{nd}^*	0.45	0.74	1.34	1.78	1.90	2.15	2.18	5.81	7.83	3.04
Γ_{fr}^*	0.36	0.65	1.56	2.40	2.27	2.38	2.10	7.96	15.23	5.56
Γ^*	0.81	1.39	2.90	4.18	4.17	4.53	4.28	13.77	23.06	8.60
Ω^*	0.46	0.50	0.57	0.66	0.75	0.77	0.82	0.85	0.83	0.82
c	0.130	0.235	0.525	0.742	0.798	0.850	0.833	1.927	2.702	3.354
f	5.75	9.91	18.12	22.19	24.40	26.55	29.95	38.12	30.23	27.82
$c/(ft_c)$	1.013	1.066	1.302	1.503	1.470	1.439	1.250	2.266	4.017	5.419
E_{11}	0.52	0.51	0.48	0.42	0.33	0.32	0.33	0.30	0.34	0.35
E_{22}	0.48	0.49	0.52	0.58	0.67	0.68	0.67	0.70	0.66	0.65
E_{21}	−0.19	−0.19	−0.16	−0.15	−0.14	−0.14	−0.14	−0.08	−0.06	−0.03
β_s	0.47	0.47	0.48	0.45	0.44	0.42	0.43	0.35	0.26	0.20
$NT/10^3$	200	200	300	500	500	500	500	500	500	500

TABLE 2. Summary of results for $B = 0.01$ (cumulative time averages)

C	0.500	0.600	0.700	0.750	0.775	0.800	0.825	0.850	0.875	0.900
τ^*_{21}	0.52	0.80	1.47	1.96	2.19	2.16	2.06	1.99	1.78	1.93
τ^*_{11}	1.09	1.66	3.21	4.46	4.99	4.78	4.32	3.94	3.28	3.56
τ^*_{22}	0.96	1.57	3.09	4.49	5.27	5.87	6.64	7.66	8.73	9.61
T^*_t	0.10	0.10	0.14	0.16	0.16	0.17	0.17	0.18	0.25	0.40
T^*_r	0.08	0.09	0.13	0.14	0.15	0.13	0.12	0.11	0.09	0.13
T^*	0.18	0.19	0.27	0.30	0.31	0.30	0.29	0.29	0.34	0.53
V^*	0.06	0.11	0.26	0.41	0.49	0.50	0.50	0.50	0.46	0.53
V/T	0.35	0.56	0.98	1.36	1.58	1.68	1.77	1.76	1.25	0.99
Γ^*_{nd}	0.27	0.40	0.65	0.79	0.84	0.80	0.76	0.73	0.70	0.92
Γ^*_{fr}	0.25	0.42	0.84	1.18	1.35	1.35	1.28	1.23	1.03	0.95
Γ^*	0.52	0.82	1.49	1.97	2.19	2.15	2.04	1.96	1.73	1.87
Ω^*	0.47	0.46	0.46	0.47	0.49	0.57	0.65	0.72	0.78	0.79
c	0.65	1.00	1.65	2.08	2.27	2.40	2.57	2.81	3.09	3.38
f	3.68	4.91	6.18	6.42	6.46	6.73	7.01	7.16	7.46	9.18
$c/(ft_c)$	1.59	1.83	2.40	2.91	3.16	3.21	3.30	3.53	3.72	3.31
E_{11}	0.51	0.50	0.50	0.50	0.49	0.46	0.43	0.41	0.40	0.44
E_{22}	0.49	0.50	0.50	0.50	0.51	0.54	0.57	0.59	0.60	0.56
E_{21}	−0.15	−0.15	−0.13	−0.11	−0.10	−0.09	−0.08	−0.06	−0.05	−0.04
β_s	0.48	0.48	0.46	0.44	0.44	0.44	0.43	0.42	0.42	0.42
$NT/1000$	100	100	100	100	100	50	50	50	50	100

TABLE 3. Summary of results for $B = 0.0707$ (cumulative time averages)

(*a*)	C	0.775	0.800	0.825	0.850	0.875	0.900
	$B = 0.001$	5.51	7.78	14.35	97.81	198.36	304.00
	$B = 0.01$	4.07	4.58	4.24	13.85	23.64	8.95
	$B = 0.0707$	2.19	2.16	2.06	1.99	1.78	1.93
	n_{21}	0.214	0.299	0.458	0.913	1.101	1.198
	a_{21}	1.332	1.038	0.576	0.187	0.112	0.061
(*b*)	C	0.775	0.800	0.825	0.850	0.875	0.900
	$B = 0.001$	6.79	9.53	15.33	461.85	2325.0	4501.0
	$B = 0.01$	5.69	6.27	5.87	18.16	44.09	56.64
	$B = 0.0707$	4.99	4.78	4.32	3.94	3.28	3.56
	n_{11}	0.072	0.163	0.301	1.127	1.547	1.684
	a_{11}	4.103	3.056	1.763	0.157	0.047	0.034
(*c*)	C	0.775	0.800	0.825	0.850	0.875	0.900
	$B = 0.001$	18.50	25.56	45.90	2172.10	12370	24275
	$B = 0.01$	14.16	16.16	13.41	63.43	159.00	236.84
	$B = 0.0707$	5.27	5.87	6.64	7.66	8.73	9.61
	n_{22}	0.290	0.341	0.456	1.332	1.709	1.845
	a_{22}	2.837	2.684	1.854	0.189	0.081	0.063

TABLE 4. Fitting of results into a power law form $\tau^*_{ij} = a_{ij}(C)B^{-n_{ij}(C)}$. (*a*) τ^*_{21}, (*b*) τ^*_{11}, (*c*) τ^*_{22}.

REFERENCES

ALLEN, M. P. & TILDESLEY, D. J. 1988 *Computer Simulation of Liquids*. Oxford University Press.

BABIĆ, M. 1988 Discrete particle numerical simulation of granular material behavior. *Rep.* 88-11. Department of Civil and Environmental Engineering, Clarkson University, Potsdam, New York.

BABIĆ, M. 1989 Contact stress in granular materials. *Rep.* 89-1. Department of Civil and Environmental Engineering, Clarkson University, Potsdam, New York.

BAGNOLD, R. A. 1954 Experiments on gravity-free dispersion of large solid spheres in a newtonian fluid under shear. *Proc. R. Soc. Lond.* A **225**, 49–63.

CAMPBELL, C. S. 1982 Shear flows of granular materials. Ph.D. thesis, California Institute of Technology, Pasadena, California.

CAMPBELL, C. S. & BRENNEN, C. E. 1985*a* Chute flows of granular materials: some computer simulations. *J. Appl. Mech.* **52**, 172–178.

CAMPBELL, C. S. & BRENNEN, C. E. 1985*b* Computer simulation of granular shear flows. *J. Fluid Mech.* **151**, 167–188.

CAMPBELL, C. S. & GONG, A. 1986 The stress tensor in a two-dimensional granular shear flow. *J. Fluid Mech.* **164**, 107–125.

CHRISTOFFERSEN, J., MEHRABADI, M. M. & NEMAT NASSER, S. 1981 A micromechanical description of granular material behavior. *J. Appl. Mech.* **48**, 339–344.

CUNDALL, P. A., DRECHER, A. & STRACK, O. D. L. 1982 Numerical experiments in granular assemblies: measurements and observations. In *Deformation and Failure of Granular Materials* (ed. P. A. Vermeer & H. J. Luger), pp. 255–270. Rotterdam: Balkema.

CUNDALL, P. A. & STRACK, O. D. L. 1979*a* A discrete numerical model for granular assemblies. *Géotechnique* **29**, 47–65.

CUNDALL, P. A. & STRACK, O. D. L. 1979*b* The distinct element method as a tool for research in granular media. Part II. Report to National Science Federation, Department of Civil and Mineral Engineering, University of Minnesota, Minneapolis, Minnesota.

CUNDALL, P. A. & STRACK, O. D. L. 1983 Modeling of microscopic mechanisms in granular material. In *Mechanics of Granular Materials: New Models and Constitutive Equations* (ed. J. T. Jenkins & M. Satake), pp. 137–149. Elsevier.

Drecher, A. & de Josselin de Jong, G. 1972 Photoelastic verification of a mechanical model for the flow of granular material. *J. Mech. Phys. Solids* **20**, 337–351.

Hopkins, M. A. 1987 Particle simulation. *Rep.* 87-7, Clarkson University, Potsdam, New York.

Hopkins, M. A. & Shen, H. H. 1988 A Monte Carlo simulation of a simple shear flow of granular materials. In *Micromechanics of Granular Materials* (ed. M. Satake & J. T. Jenkins), pp. 349–358. Elsevier.

Jenkins, J. T. & Richman, M. W. 1985*a* Grad's 13-moment system for a dense gas of inelastic spheres. *Arch. Rat. Mech. Anal.* **87**, 355–377.

Jenkins, J. T. & Richman, M. W. 1985*b* Kinetic theory for plane shear flows of a dense gas of identical, rough, inelastic, circular disks. *Phys. Fluids* **28**, 3485–3494.

Jenkins, J. T. & Richman, M. W. 1988 Plane simple shear flow of smooth, inelastic, circular disks: the anisotropy of the second moment in the dilute and dense limit. *J. Fluid Mech.* **192**, 313–328.

Jenkins, J. T. & Savage, S. B. 1983 A theory for the rapid flow of identical, smooth, nearly elastic, spherical particles. *J. Fluid Mech.* **130**, 187–202.

Johnson, P. C. & Jackson, R. 1987 Frictional–collisional constitutive relations for granular material, with application to plane shearing. *J. Fluid Mech.* **176**, 67–93.

Lun, C. K. K., Savage, S. B., Jeffrey, D. J. & Chepurney, N. 1984 Kinetic theories for granular flow: inelastic particles in a Couette flow and slightly inelastic particles in a general flowfield. *J. Fluid Mech.* **140**, 223–256.

Mindlin, R. D. & Deresiewitz, H. 1953 Elastic spheres in contact under varying oblique forces. *J. Appl. Mech.* **20**, 327–344.

Sanders, B. E., Hopkins, M. A. & Ackermann, N. L. 1988 Physical experiments and numerical simulation of two dimensional chute flow. In *Micromechanics of Granular Materials* (ed. M. Satake & J. T. Jenkins). Elsevier.

Savage, S. B. 1982 The mechanics of rapid granular flow. *Adv. Appl. Mech.* **24**, 289–366.

Savage, S. B. 1988 Streaming motions in a bed of vibrationally fluidized dry granular material. *J. Fluid Mech.* **194**, 457–478.

Spencer, A. J. M. 1981 Deformation of an ideal granular material. In *Mechanics of Solids, Rodney Hill 60th Anniversary Volume* (ed. H. G. Hopkins & J. J. Sewell). Pergamon.

Strack, O. D. L. & Cundall, P. A. 1978 The distinct element method as a tool for research in granular media. Part I. Report to National Science Foundation, Department of Civil and Mineral Engineering, University of Minnesota, Minneapolis, Minnesota.

Walton, O. R. & Braun, R. L. 1985 Viscosity, granular temperature and stress calculations for shearing assemblies of inelastic, frictional disks. *J. Rheol.* **30**, 949–980.

Walton, O. R. & Braun, R. L. 1987 Stress calculations for assemblies of inelastic spheres in uniform shear. *Acta Mech.* **63**, 73–86.